Chapter 13
Spinoptics in plasmonics

Erez Hasman* and Vladimir Kleiner

Micro and Nanooptics Laboratory, Faculty of Mechanical Engineering, and Russell Berrie Nanotechnology Institute, Technion-Israel Institute of Technology, Haifa 32000, Israel

***mehasman@technion.ac.il**

Abstract We review our work on effects of spin-symmetry breaking in nanoscale structures caused by spin-orbit interaction. The spin-based effects offer an unprecedented ability to control light and its polarization state in nanometer-scale optical devices, thereby facilitating a variety of applications related to nano-photonics. The polarization-dependent effects are considered as result of a geometric phase arising from the interaction of light with an anisotropic and inhomogeneous nanoscale structure. The discussed phenomena inspire one to investigate other spin-based plasmonic effects and to propose a new generation of optical elements for nano-photonic applications, as a constituent of a new branch in optics – *spinoptics*.

13.1 Introduction

The interaction of light with metallic subwavelength structures exhibits various anomalous effects such as extraordinary optical transmission[1] and beaming [2]. These effects have been elegantly explained by a mechanism involving the coupling of light to collective surface-confined electronic oscillations known as surface plasmon-polaritons (SPPs). Extensive research has been carried out in the field of electromagnetic surface waves due to its technological potential and fundamental implications. Additional exciting phenomena were studied such as unidirectional plasmon coupling [3], plasmon focusing [4,5], waveguiding and interferometry [6,7], enhanced coherent thermal emission [8,9], surface-enhanced Raman scattering [10], planar optical chirality[11,12] and super-resolution [13,14]. Apparently, the handedness of the light's polarization (optical spin up/down) may provide an additional degree of freedom in nanoscale photonics. The dynamics of spinning light was recently investigated, and the effect of spin on the trajectories of polarized light beams (spin-orbit coupling) was experimentally observed [15], with results that agree with the predictions of Berry's phase theory. In this chapter we examine the spin-orbit coupling effects that appear when a wave carrying intrinsic angular momentum (spin) interacts with a nanoscale structures which support SPP. The Berry's phase is shown to be a manifestation of the Coriolis effect

in noninertial reference frame attached to the wave. A variety of experiments demonstrate spin-dependent effects in the electromagnetic waves coupling via an anisotropic inhomogeneous nanostructure. In the Section 13.2 we present and discuss the observation of spin-dependent surface-plasmon phenomena in anisotropic nanostructures on metal surface. In the Section 13.3 we consider plasmonic nanoapertures which exhibit a crucial role of an angular momentum (AM) selection rule in a light-surface plasmon scattering process, which is accompanied by a spin symmetry breaking effect due to spin-orbit interaction. Section 13.4 is devoted to properties of plasmonic nanoapertures which demonstrate behavior that is analogous to the Aharonov-Bohm effect. In Section 13.5 properties of the nanoapertures as topological defects are considered in relation with potential spinoptical devices having a spiral point spread function. An optical spin Hall effect in this system due to spin-orbit coupling which can be observed in the far-field is then studied in detail in Section 13.6. In the final Section 13.7 observation of an optical Rashba effect - spin degeneracy breaking due to spin-orbit interaction - in thermal radiation emitted from an inhomogeneous anisotropic 2D lattice composed of coupled antennas is presented. The spin split dispersion arises from the inversion symmetry violation in the lattice.

13.2 Spin-Based Plasmonic Effect in Nanoscale Structures

In this section we will describe a spin-dependent behavior of SPPs that was experimentally found in the interaction of light with metallic anisotropic and inhomogeneous nanoscale structures [16]. The anisotropic plasmonic structure under consideration is produced on top of a thin metal film evaporated onto a glass plate (Fig. 13-1a,b). The element consists of a spiral Bragg grating with a central defect, surrounded by a coupling grating, both of which were etched to a depth of 50nm by a focused ion beam (FIB). The thickness of the metal (Au) was chosen to be 100nm in order to prevent any direct transmission of light. The grating provides coupling with normally incident light at $\lambda_0 = 532nm$ to a surface-plasmon wave, while the Bragg grating with a central defect serves as a plasmonic microcavity for the surface wave. Therefore, the actual coupler period and the Bragg period were chosen to be 0.5μm and 0.25μm, respectively. The outer diameter of the structure of 10μm and the small radius of the spiral cavity r_0 = 1.32μm are consistent with the surface plasmon propagation length [17] $L_c \propto 1/\mathrm{Im}(k_p)$, which is about 3μm for gold at this wavelength.

The structure was illuminated by circularly polarized light which is denoted henceforth with a spin state $|\pm_\pm\rangle$, where $|\pm_+\rangle = 2^{-1/2}(1 \quad -i)^T$ stands for right-handed circularly polarized light and $|\pm_-\rangle = 2^{-1/2}(1 \quad i)^T$ for left-handed circularly

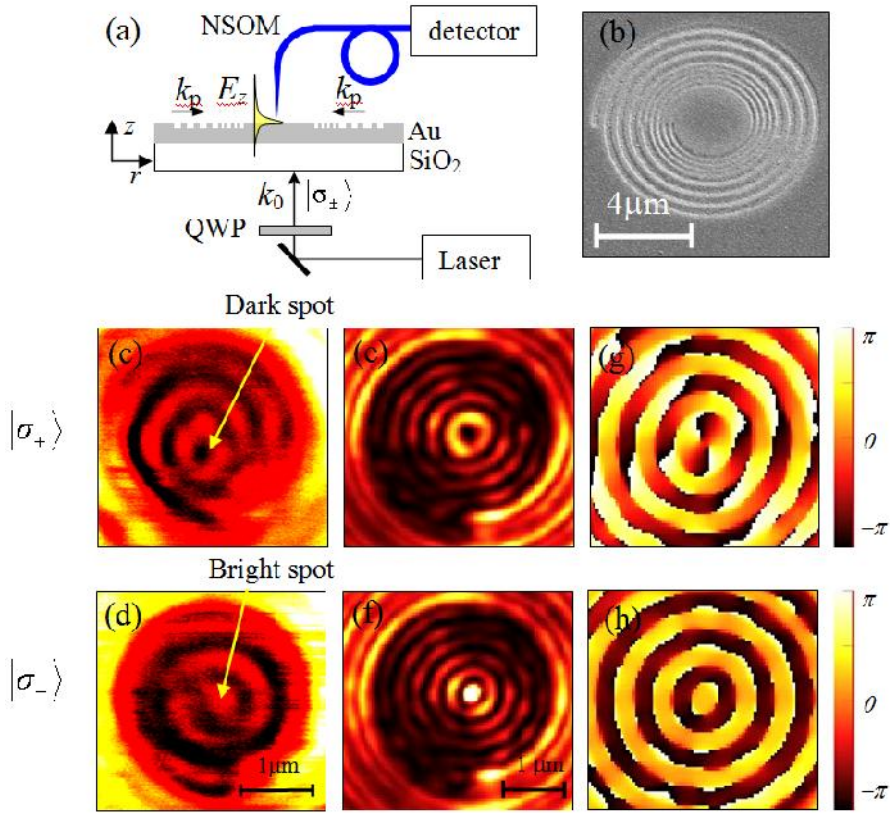

Fig. 13-1 Spin-dependent geometric phase in the spiral plasmonic structure. a) The geometry of the structure (side view) and the optical setup. The Quarter Wave Plate (QWP) was used to generate a circularly polarized illumination, which was partially coupled to the SPP mode in the cavity – E_z. b) Scanning electron microscope (SEM) picture of the spiral plasmonic cavity. c,d) Intensity distribution in the cavity measured by a NSOM for $|\pm_+\rangle$ and $|\pm_-\rangle$ illumination, respectively. e,f) Calculated intensity in the cavity for $|\pm_+\rangle$ and $|\pm_-\rangle$ illumination. (g,h) Calculated phase in the cavity for $|\pm_+\rangle$ and $|\pm_-\rangle$ illumination.

polarized light. Figure 13-1a demonstrates the intensity in the near-field of the plasmonic cavity that was measured by a near-field scanning optical microscope (NSOM) in a non-contact mode. The captured intensity distribution is presented in Fig. 13-1c,d. The near-field intensity distribution which calculated by a finite difference time domain (FDTD) algorithm is depicted in Fig. 13-1e,f. Surprisingly, the measured as well as the calculated intensity distribution exhibits a strong dependence on the incident spin. An annular ring structure with a dark spot in the center for $|\pm_+\rangle$ illumination and with a bright spot for $|\pm_-\rangle$ illumination indi-

cates coupling to different spiral plasmonic modes. The origin of the spin-dependent change in the near-field intensity distributions lies in the phase of the excited plasmonic mode. This phase has been verified by FDTD calculation (see Fig. 13-1g,h) and was found to correspond to a spiral mode $\exp(il\varphi)$, where φ is the azimuthal angle, with topological charge $l = -2$ for $|\pm_+\rangle$ and $l = 0$ for $|\pm_-\rangle$ illumination. The origin of the spin-dependent phase could be elucidated by use of

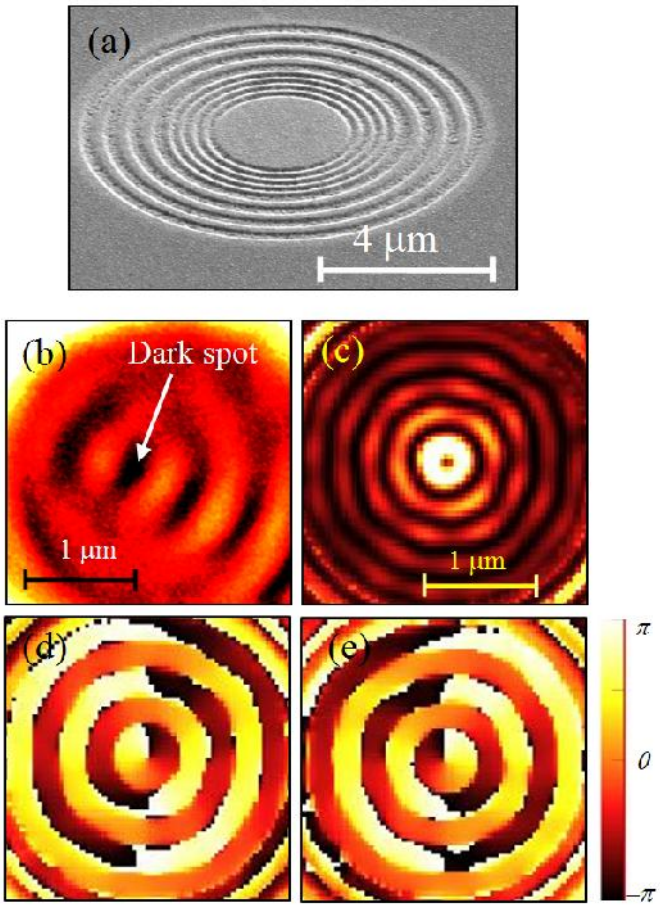

Fig. 13-2 Plasmonic field distribution in the circular cavity. a) SEM picture of the circular structure. b) Measured intensity distribution in the near-field for $|\pm_+\rangle$ illumination. An identical intensity distribution was obtained for $|\pm_-\rangle$. c) Calculated intensity distribution for $|\pm_+\rangle$. d,e) Calculated E_z field phase inside the cavity for $|\pm_+\rangle$ and $|\pm_-\rangle$ illumination, respectively.

a simpler structure with full rotational symmetry (see Fig. 13-2a). This structure consisted of concentric rings with the same depth and pitch as before and a central circular microcavity (r_0 = 1. 2μm). The eigenmodes of such a circular plasmonic cavity are given by,

$$\mathbf{E}_{l,p}(¨,r) = E_0 \exp(ik_z z)\exp(il¨)\,\boldsymbol{J}_l(k_p r)\hat{\mathbf{z}}, \tag{13-1}$$

where k_z is the wavenumber perpendicular to the surface direction, k_p is the radial wavenumber; ¨ , r and z are the cylindrical coordinate set, l is the topological charge and E_0 is a constant. The notation $\boldsymbol{J}_l$ stands for the l-order Bessel function of the first kind. The plasmonic in-plane wavenumber is given approximately by $k_p \sim k_0\sqrt{£/(1+£)}$, where £ is the dielectric constant of the metal $(\mathrm{Re}(£)<-1)$ and $k_0 = 2®/{}^{a}_{0}$ is the wavenumber of the incident light. The wavenumber in the z direction is expressed by $k_z^2 + k_p^2 = k_0^2$ and consequently is purely imaginary ($k_p > k_0$). Equation (1) represents an optical scalar vortex with a topological charge, l, which is associated with the optical angular momentum of the mode and corresponds to appropriate phase boundary conditions. The experimental near-field intensity distribution presented in Fig. 13-2b indicates a non-zero topological charge, which corresponds to a helical phase distribution for both $|±_+\rangle$ and $|±_-\rangle$ illumination. The FDTD calculation presented in Fig. 13-2d,e clear indicates that helicity of the phase equals to $l = -±_±$, where $±_+ = 1, (±_- = -1)$ stands for the spin state $|±_+\rangle, (|±_-\rangle)$, respectively. This is evidence of a selective spin-dependent coupling to a single cavity mode induced by the structure. The existence of a spin-dependent spiral phase can be elucidated by analyzing the coupling mechanism between incident light with a specific spin and a surface plasmon cavity mode.

In plasmonic systems, when a coupling structure is illuminated by an arbitrarily polarized beam, the surface waves are excited via transverse magnetic (TM) polarization, corresponding to the magnetic field parallel to the grooves direction [17]. The propagation direction of the resulting plasmonic surface wave is perpendicular to the grooves whereas its polarization is linear in the vertical direction, E_z. If the direction of the grating's grooves varies azimuthally, the coupling of an incident plane wave to a surface wave takes place within a space-variant local direction. This non-trivial simultaneous manipulation in the space of polarizations and in the space of directions one can describe using geometric representation upon the Majorana sphere [18,19]. In this scheme, polarized light is characterized by two dots on a unit sphere in the direction space (x,y,z), i.e., by two vectors, **u** and **v**, which point to these dots from the origin. Their bisector unit vector, **n**, coincides with the propagation direction of the wave, while its sign corresponds to the helicity of the polarization ellipse. For pure circular polarizations the bisector can be denoted as $±_±\mathbf{n}$. The projections of the dots onto the plane perpendicular to **n**

denote the two foci of the corresponding polarization ellipse. The physical significance of this representation is that it provides a method to evaluate a geometric Berry phase [20-22] for complex fields whose polarization and direction have been modified.

Let us consider right-handed circularly polarized illumination $|E_{ext}\rangle = E_0|\pm_+\rangle$ impinging upon the element depicted in Fig. 13-2a from the bottom. Here E_0 is the amplitude of the field, which can be taken as one for brevity purposes. The circularly polarized incident beam, propagating along the z direction, can be depicted on the Majorana sphere by vectors **u** and **v**, which coincide at the north pole (see Fig. 13-3). The evanescent vertically polarized electric field that propagates on the

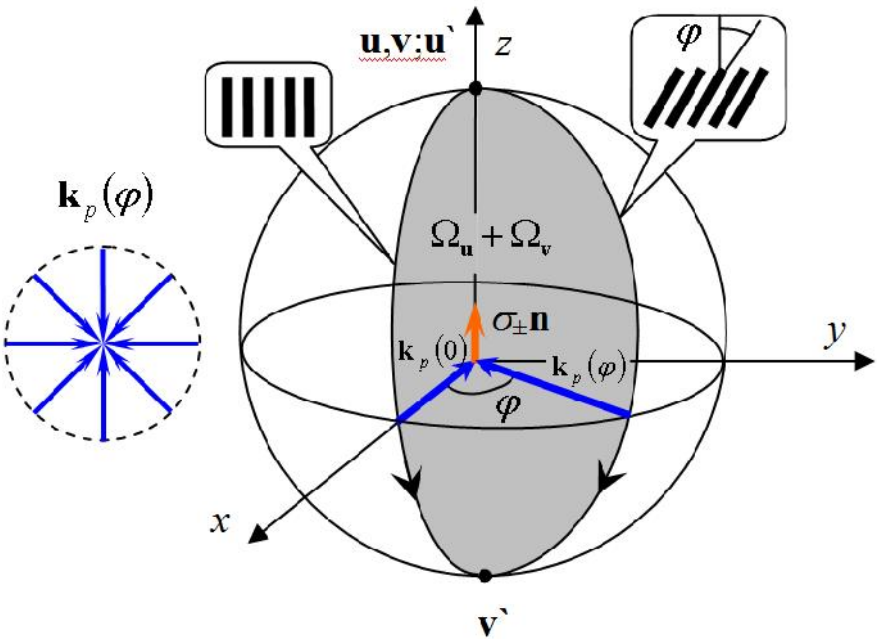

Fig. 13-3 Graphical representation of the geometric phase on the Majorana sphere. Geometric phase induced by the interaction of light with an anisotropic inhomogeneous structure is equal to half of the area enclosed by the two geodesics that correspond to different propagation directions, k_p of the excited SPPs (gray area). The variation of the propagation wavevector $\mathbf{k}_p(\ddot{})$ along the element is depicted in the small picture by blue arrows.

metal surface in a radial direction is consequently represented by a vector **u`**, which still points to the north pole, and a vector **v`** which now points to the south pole. The interaction of light with a coupling grating whose local orientation is ¨ can then be defined by a geodesic arc connecting the north pole with the south

pole that intersects the *xy* plane at angle ¨ (see Fig. 13-3). The Berry phase in our specific case is geometrically associated with the area enclosed on the Majorana sphere by the paths of vectors **u** and vector **v**, explicitly, $¤_g = -(\Omega_{\mathbf{u}} + \Omega_{\mathbf{v}})/2$. Since the vector **u** is static, the Berry phase between the fields at two different azimuthal locations will be given simply as half of the area between two corresponding geodesics, which yields $¤_g = -¨$. In the opposite case, when left-handed circularly polarized light is applied, i.e., $|E_{ext}\rangle = E_0|±_-\rangle$, the picture on the sphere will be reversed. The initial state will be denoted by vectors **u** and **v** both pointing to the south pole, and the final state will be defined by **u`** pointing to the south pole and **v`** pointing to the north pole. In the second case, the path traversed on the Majorana sphere is in the reverse direction, which corresponds to the positive geometric phase, $¤_g = ¨$. The general case, therefore, can be given by $¤_g = -±_±¨$. Note that this phase results from the spin-orbit angular momentum coupling due to the space-variant polarization state and directional manipulations and is therefore geometric in nature. The appearance of the geometric phase in our experiment resulted from the SPP excitation by a spatially rotated grating and resembles the phase delay that arises when circularly polarized light is transmitted through a rotated polarizer [21,22]. This phase is linear with ¨ and spirals around the center of the structure, giving rise to a phase singularity with a topological charge $l = -±_±$; these properties explain the results presented in Fig. 13-2.

The intensity distributions in the cavity described above for incident spins $±_+$ and $±_-$ are indistinguishable, as opposed to the experimental results obtained in the spiral cavity (see Fig. 13-1). In the latter, in addition to the geometric phase of the SPPs due to a polarization-dependent coupling, a dynamic phase arises as a result of a space-variant path difference. This dynamic phase is induced by the grooves' spiral pitch. The overall phase in the spiral cavity is the sum of the geometric and dynamic phases, $¤ = ¤_g + ¤_d$ and the total topological charge of the plasmonic vortex is $l = -(±_± + m)$, where *m* is the spiral pitch in the units of SPP wavelength. For the specific case when *m*=1, the microcavity mode obeys the form of $\boldsymbol{J}_0(k_p r)$ for $|±_-\rangle$ and of $\exp(-i2¨)\boldsymbol{J}_2(k_p r)$ for $|±_+\rangle$. Consequently, for $|±_-\rangle$ illumination the resultant field distribution possesses no phase singularity in the center, as opposed to the $|±_+\rangle$ illumination case, which agrees with the experimental results presented in Fig. 13-1. The formation of the geometric phase is, therefore, the origin of the spin-dependent intensity distribution in the spiral cavity, and may lead to other spin-based phenomena in plasmonic systems.

One of the possible implementations of the plasmonic geometric phase could be a spin-dependent plasmonic focusing lens. Fig. 13-4e presents an appropriate structure that consisted of a 150nm-thick gold film with a hemi-circular coupling

grating with the inner radius of r_0 = 1.64 μm followed by a Bragg grating on the outer side. In experiment the structure was illuminated from the bottom with $|\pm_+\rangle$ and $|\pm_-\rangle$ plane waves and the intensity distribution was collected by the NSOM tip. The measured intensity of the plasmonic wave is shown in Fig 13-4a,b. The most interesting feature in this intensity distribution is a spin-dependent transverse shift of the focus which one can easily observe by comparing the cross-sections of the spots (Fig. 13-4c). This shift can be regarded as a manifestation of the optical Magnus effect [23,24] and the optical spin Hall effect [25, 26] which arises in the

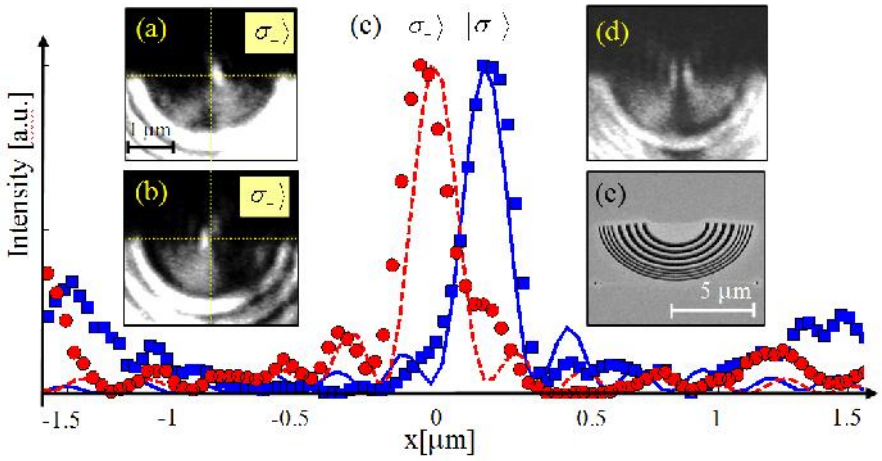

Fig. 13-4 Spin-dependent plasmonic lens based on a geometric phase. a, b) The intensity distributions measured by a NSOM for $|\pm_+\rangle$, and $|\pm_-\rangle$ illumination, respectively. c) The transverse cross-sections of the measured intensity distributions in the focal plane of the lens for $|\pm_+\rangle$ (blue squares) , $|\pm_-\rangle$ (red circles) illumination, respectively. FDTD calculation is plotted for each polarization (solid blue line - $|\pm_+\rangle$; dashed red line - $|\pm_-\rangle$). The cross-sections in (c) were measured along the horizontal dashed lines depicted in a) and b). d) The intensity distribution measured by NSOM for $|\pm_+\rangle + |\pm_-\rangle$ (linearly polarized) illumination. e) The SEM picture of the element.

system due to a spin-orbit coupling producing a spiral geometric phase. The experimental results are supported by the FDTD numerical simulation which are also depicted in the Fig. 13-4c. The focal shift corresponds to the spin-dependent spiral phase modification due to the Berry phase and can be estimated by $\Delta x \approx r_0 \left| k_p^{-1} \right| \nabla(\pm_{\pm}^{\cdot\cdot}) = \pm_{\pm} \left| k_p^{-1} \right|$, ($\Delta x \approx 160nm$). The observed shift of the focal intensity distribution is about 200 nm which is in good agreement with the above estimation as well as with the FDTD results (see Fig. 13-4c). The slight deviation of

the measured results from the simulation can be attributed to the modified dispersion relation of the SPPs due to impurities caused by the fabrication process. This geometric effect is exceptionally pronounced when linearly polarized light (the superposition of spin $|\pm_+\rangle$ and $|\pm_-\rangle$ beams) is incident upon the structure. In this case, the focal spot is split in the lateral direction (see Fig. 13-4d) and clearly reminds us the effect of spin-dependent electron beam splitting in the classic Stern-Gerlach experiment [27, 28].

13.3 Optical Spin Symmetry Breaking in Nanoapertures

The dynamics of various physical systems, including optical systems, are substantially characterized by their AM. The AM of an optical beam comprises the spin component, associated with the handedness of the circular polarization, and the orbital angular momentum (OAM), associated with a spiral phase front [29-32]. In a paraxial beam with a spiral phase distribution ¤ $\propto l^{¨}$, the total AM per photon, in units of $\hbar$ (normalized AM), was shown to be $j=(\pm+l)$, where $\pm=1$ stands for the spin state $|\pm_+\rangle$ and $\pm=-1$ stands for the spin state $|\pm_-\rangle$ [33]. In accordance with fundamental physical principles, resonant excitation of an electromagnetic eigenmode requires that the exciting wave match the excited mode both with its linear and angular momentum. This required matching imposes certain restrictions on the excitation process – selection rules. Likely the simplest plasmonic nanoscale structure, which demonstrates these common rules is a nanoaperture in a
thin metal film. Let consider a matrix consisted of annular apertures surrounded by a shallow spiral periodic corrugation. In the experiment [34] a structure with the inner and the outer radii of the ring slit apertures of 250 and 350 nanometers, respectively, spiral corrugation with a period of 500nm and a pitch of 2 periods, and depth of 70nm was milled by a FIB into a 200nm thick gold film evaporated onto a glass wafer (see Fig. 13-5b). Transmission of circularly polarized light through the structure is strongly affected by relationship between helicity of illuminating light and handedness of the spirals. A picture of the transmitted light for the spin states $|\pm_+\rangle$ and $|\pm_-\rangle$, and for the linear polarization $2^{-1/2}\left(|\pm_+\rangle+|\pm_-\rangle\right)$is presented in Fig. 13-5a. The experimental results show that when the incident spin is opposite to the handedness of the spiral grating, the intensity of the transmitted light is enhanced. Accordingly, the word "SPiN" written with right-handed spirals is lit up when illuminated by $|\pm_-\rangle$ light. For $|\pm_+\rangle$ illumination, the contrast is reversed. A spectral transmission through a similarly structured array of only right-handed spirals, normalized by transmission through a annular aperture array with-

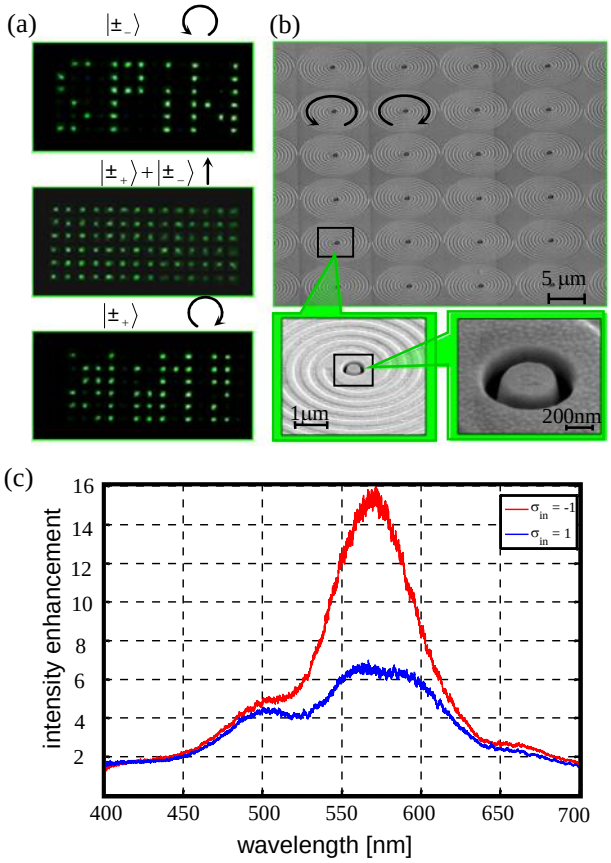

Fig. 13-5 Spin-dependent transmission through annular nanoapertures. a) light transmission measured from the element for $|\pm_-\rangle$, $|\pm_+\rangle+|\pm_-\rangle$ and $|\pm_+\rangle$ illuminations. b) SEM picture of the element used in the experiment. Spiral corrugations are either left-handed or right-handed, depicted with a counterclockwise or clockwise arrow, respectively. The magnified SEM pictures of a single element and a coaxial nanoaperture are also presented. c) spectral transmission enhancement for $|\pm_-\rangle$ (red line) and $|\pm_+\rangle$ (blue line). The spectrum was normalized by the transmission measured for annular apertures without corrugations.

out corrugations manifest a clearly observed resonant peak for $|\pm_-\rangle$ illumination around 570 nm. The light transmission at the peak was found to be enhanced by factor of 16 relative to an uncorrugated aperture array. The spectral transmission of a $|\pm_+\rangle$ illumination does not exhibit any substantial resonance.

The excitation of electromagnetic eigenmodes inside a nanoaperture by surface waves is constrained by the AM selection rule, which is given by

$$l_{SM} = l_{GM}, \tag{13-2}$$

where l_{SM} and l_{GM} are the normalized OAM of the surface mode and guided mode inside the annular structure, respectively. A conceptual scheme of the transmission mechanism is depicted in Fig. 13-6. The annular nanoapertures can

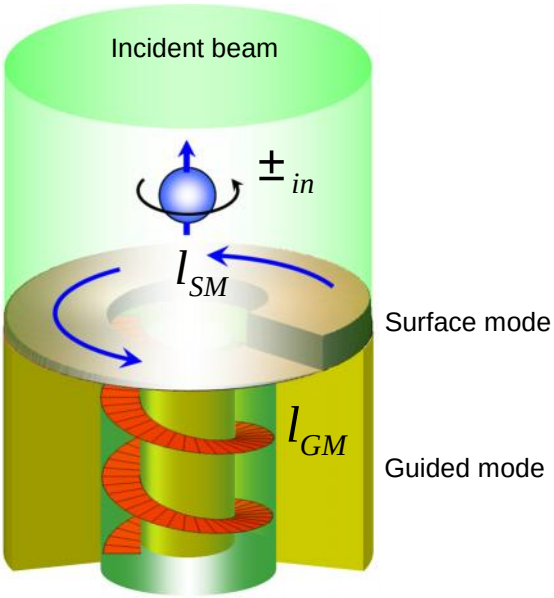

Fig. 13-6 The mechanism of the nanoaperture's excitation controlled by the AM selection rules. The incident beam bears the intrinsic angular momentum of $\pm_{in}$. The excited surface mode acquires the orbital angular momentum of l_{SM} as a result of the plasmonic spin-orbit interaction. The guided mode with l_{GM} is excited only if the selection rule is satisfied.

be designed to be a single mode system; for example, as in this case possessing a single allowed excitation for $l_{GM} = \pm 1$. This is a useful advantage of the annular apertures. The spiral corrugation couples the incident light into a plasmonic wave

and induces a dynamic spiral phase according to the spiral grating pitch, l_S. In the described structure the spiral corrugation adds to the surface mode a spiral phase with $l_S = 2$. Experiment shows that *only* $l_S = 2$ provides spin-dependent transmission enhancement through the apertures. The observed exceptional transmission enhancement indicates that the eigenmode of the annular waveguide is properly excited by a surface mode. The apparent difference between $l_{GM} = \pm 1$ and the spiral charge $l_S = 2$ of the surface mode leads one to assume that another mechanism induced an additional spin-dependent spiral phase that compensated the excess of AM on the left side of the selection rule in Eq. (13-2). This phase modifies the complete OAM of the surface mode to be $l_{SM} = \pm_{in} + l_S$, ($\pm_{in}$ is the incident spin) which now perfectly satisfies the AM selection rule of the system. Thus, the incident spin is converted into the OAM, conserving the total AM of the system. The process by which an intrinsic property of light is coupled to an extrinsic property of a plasmonic field will be referred here to *plasmonic spin-orbit interaction*. This interaction occurs in anisotropic and inhomogeneous structures and is manifested by a geometric Berry phase arising in the system [15,16, 36,37].

The above effect can be regarded as a spatial angular Doppler effect (ADE) [38]. In analogy with a *temporal* ADE, where an observer at a reference frame rotating with a rate Ω_t registers a spin-dependent temporal frequency shift [39], here a spatial rotation of the periodic surface corrugation with a rate of $\Omega_¶$ induces a spin-dependent *spatial* frequency shift. Accordingly, the geometric phase arising from this spatial frequency modulation can be easily calculated to be $¤_g = -\pm_{in}\int \Omega_¶ \, d¶$, where the rotation of the grating is given by $\Omega_¶ = d¯/d¶$, the angle $¯$ indicates the local groove's orientation, and $¶$ stands for a spatial coordinate. In the structure presented in Fig. 13-5b where $¶ = ¨$, the geometric phase is simply given by the spin-dependent spiral phase $¤_g = -\pm_{in}¨$ producing the required additional OAM for the surface wave to satisfy the AM selection rule (Eq. (2)). Note that while polarization and chirality effects in anisotropic inhomogeneous nanoscale structures were investigated previously [40-43], the mechanism of spin-orbit interaction was not distinguished.

It is very helpful to compare the behavior of the spiral structure discussed above with properties of the annular aperture fitted with in a circularly symmetric (achiral) corrugation using incident beam with OAM . The circular symmetry of the coupling corrugation does not induce a dynamic phase, which means that $l_S = 0$. However, due to the spin-orbit interaction, the incident spin induces a spiral Berry phase, and, as before, is converted to the OAM component of the surface mode. The external spiral phase modifies the complete OAM of the surface mode to be $l_{SM} = \pm_{in} + l_{ext}$. Therefore, when the external OAM is zero, the resulting surface mode AM is $l_{SM} = \pm 1$, in which case the selection rule is *always* satisfied

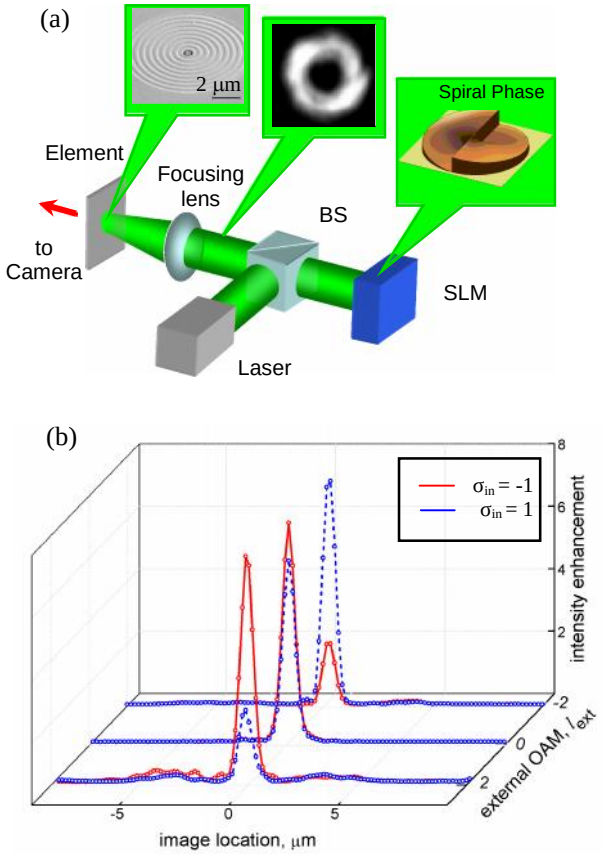

Fig. 13-7 The removal of the spin-degeneracy in circular corrugation by use of externally induced OAM. a) experimental setup. A laser beam is modulated by a spatial light modulator (SLM) to obtain a spiral phase and then incident through a beam splitter (BS) onto a coaxial aperture with circular corrugation. The transmitted light is captured in the image plane by the camera. The spiral phase with $l_{ext} = 2$, the measured intensity distribution across the incident beam, and the SEM picture of the element are presented in the figure. b) intensity distribution cross-sections captured by the camera for different l_{ext}. The blue dashed lines correspond to $|\pm_+\rangle$ illumination and red solid lines correspond to $|\pm_-\rangle$ illumination. The intensity is normalized by the transmission measured via a annular aperture without the surrounding corrugation (the horizontal dimension is scaled according to the optical magnification).

and the transmission of the element is undistinguished for distinct spin states. Moreover, providing an external spiral phase of $l_{ext} = 2$, the AM of the surface mode will be either 1 or 3 for an incident spin $|\pm_-\rangle$ or $|\pm_+\rangle$, respectively. For

$l_{ext} = -2$ the surface mode AM will be correspondingly, -3 for $|\pm_-\rangle$ and -1 for $|\pm_+\rangle$. As before, the best overlapping of the surface mode and the guided mode is obtained for $l_{SM} = \pm 1$; therefore, the transmitted intensity will be strongly dependent upon the incident spin.

Figure 13-7b shows the measured transmissions of a laser light at wavelength 532 nm by use of a spatial light modulator (SLM) generating a beam with OAM for various combinations of l_{ext} and $\pm_{in}$. The transmission ratio of the two spin states is shown to be approximately 3 which is close to the ratio measured with the spiral corrugations. Thus, the suggested AM selection rule is verified for systems of substantially different symmetry.

Additional understanding of the AM evolution in the enhanced resonant transmission can be obtained by analyzing the AM of the light scattered from the nanoaperture. To do this, one should investigate the scattered light far behind the element. The transverse electric field component of the guided mode [44] with $l_{GM} = 1$, can be described by the Jones vector $\mathbf{E}_r^{GM} = (E_x \quad E_y)^T = E_0(r)(\cos\varphi \quad \sin\varphi)^T e^{i\varphi}$, where $E_0(r)$ is the radial field dependence. Note that the guided mode in a circular basis is given by $\mathbf{E}_r^{GM} = 2^{-1/2} E_0(r)[|\pm_-\rangle + e^{i2\varphi} |\pm_+\rangle]$. This field distribution corresponds to a vectorial vortex (see Fig. 13-8a) with a Pancharatnam topological charge of 1, resulting in a total AM of $j = 1$. As was shown [45], such vectorial vortices are unstable and collapse upon propagation. The guided mode can be verified by propagating it to the far-field and it was done in experiment (see Fig. 13-8b-e). As expected from the far-field of $\mathbf{E}_r^{GM}$, a bright and a dark spot have been observed for the left and right circular polarization components, respectively, with a good agreement between calculation and measurement. Thus, the total AM of light in the system is conserved also for the scattered light ($j = 1$).

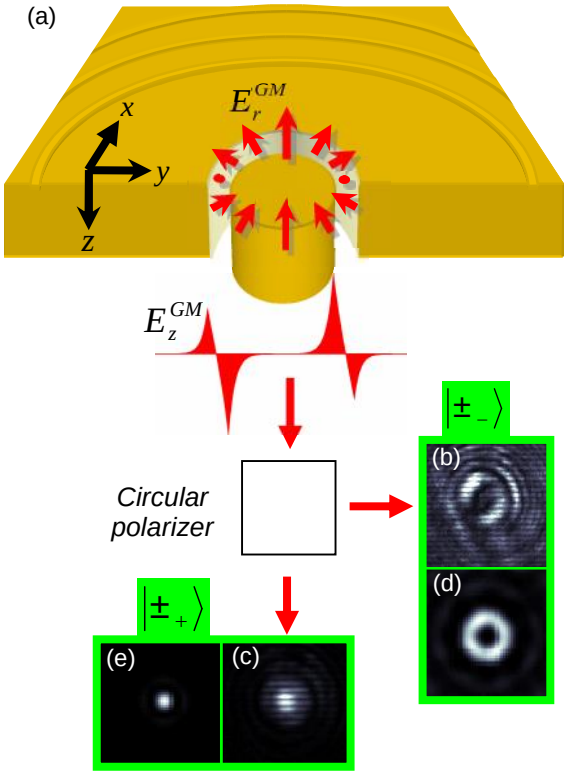

Fig. 13-8 Far-field analysis of the light scattered from the element. a) The E_z component distribution of the guided mode and the instantaneous transverse vectorial field (E_r). b,c) measured and d,e) calculated intensity distributions of the light scattered to the far-field, for light transmitted through right-handed b,d) and left-handed c,e) circular polarizer.

13.4 Plasmonic Aharonov-Bohm Effect

As it was showed in previous section the rotation of the local anisotropy axis related to the slit curvature entails correction of the momentum term in the wave equation, which results in a spiral geometric phase. The geometric phase of the surface plasmons can be directly observed via the interference pattern in the near-field by means of near-field scanning optical microscope (NSOM) [46]. The observed effect will be analyzed using the analogy of the scattering of electrons from a topological defect in the Aharonov-Bohm (AB) experiment [47]. In order to observe the surface plasmon interference in the near-field a structure onto glass sub-

strate was chosen consisting of thin (120nm) gold film with annular aperture (inner and outer radii of the aperture are 365nm and 525nm, respectively). The 320nm-wide slit has been milled in the proximity of the annular aperture to provide a reference wavefront for the interference measurement (see Fig. 13-9a,b). The structure was illuminated by a tunable laser and excited surface plasmon wave was directly probed by the 150nm aperture NSOM tip. The measured fringe pattern for incident right- and left-handed circularly polarized light ($\pm = \pm 1$) at $^{a}_{0} = 800nm$ is presented in Fig. 13-10a,b. The resulting pictures appear to be asymmetric in that an additional fringe emerge above or below the coaxial aperture according to the incident spin (see fringe analysis in Fig. 13-10c,d). It can

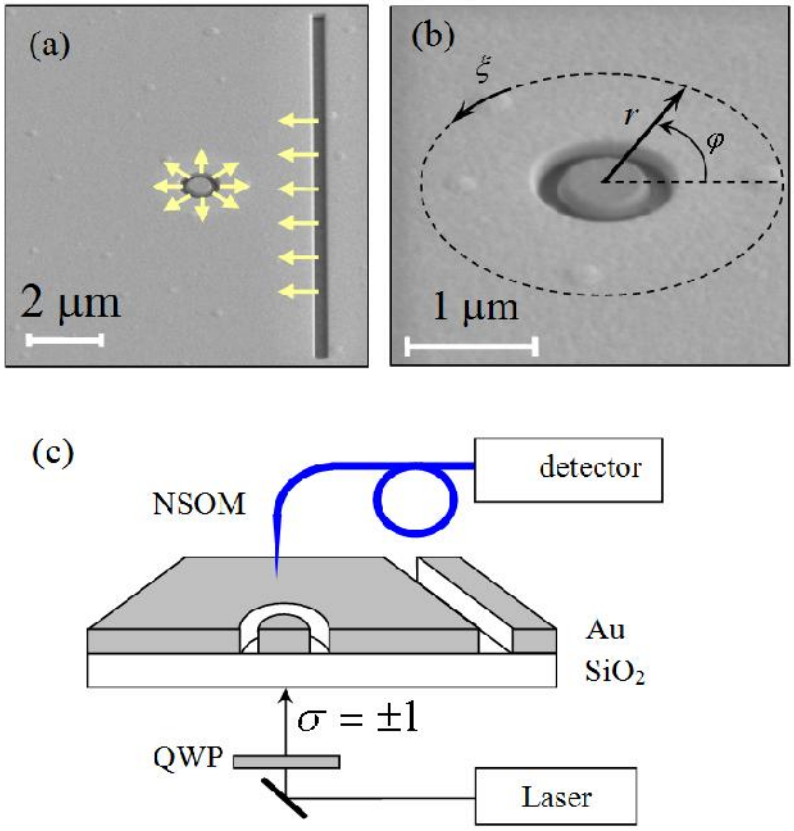

Fig. 13-9 a) SEM image of the investigated element. b) A magnified SEM image of the circular nanoslit. c) Experimental set-up. The element is illuminated from the bottom by the laser beam whose polarization was switched by a quarter-wave plate (QWP) to be $\pm = \pm 1$. The near-field intensity distribution was measured by the NSOM tip.

be concluded that a plasmonic wave scattered by the cylindrical defect acquires a phase front dislocation [46] analogous to the one obtained in a AB wavefunction [47-49]. A phase dislocation is a singular point of the field where the phase is indeterminate; therefore the field amplitude must vanish there. Such a dislocation is evidence of a spiral phase front obtained by the scattered surface plasmons. In the experiment, the additional fringe appearing in the interference pattern indicates that the topological charge of the spiral phase is ± 1, depending on the incident spin; therefore, the corresponding phase distribution is given by $¤ = -\pm ¨$, where $¨$, is the azimuthal angle (Fig. 13-9b). This phenomenon can be elucidated by considering the effect of spin-orbit coupling.

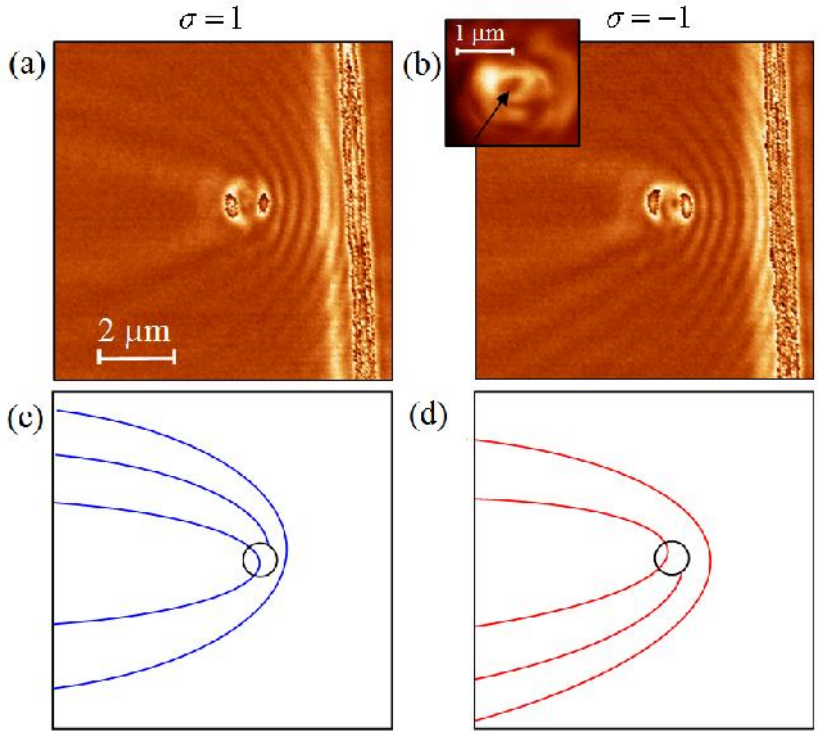

Fig. 13-10 Measured near-field intensity a) for $\pm = 1$ polarization and b) for $\pm = -1$ polarization, at $ª = 800nm$. The observed fringe maxima are presented in c) for $\pm = 1$ and in d) for $\pm = -1$ states. The black circle in c) and d) represents the location of the annular nanoslit. The inset in b) with a dark spot in the center (marked with an arrow) is the measured intensity distribution inside the circular slit.

The coupling of light to non-radiative surface modes is achieved via momentum modification by a surface defect, such as a nanoaperture [50,51]. In particular, a nanoslit introduces a momentum modification (matching) in perpendicular direction, exciting a surface wave with a phase front parallel to the slit. Moreover, only TM polarized incident waves (with an electric field perpendicular to the slit) can be efficiently coupled by the slit to surface plasmons. This polarization selectivity in SPP excitation implies highly anisotropic interaction. Due to the circular shape of the annular slit, it is convenient to analyze the wave propagation in a rotating reference frame attached to a local anisotropy axis [46, 52, 53]. For the observer moving along a path with radius r the local structure (slit) orientation appears to be rotated with the rate $\Omega = d\bar{}/d\xi = 1/r$ where $\bar{}(\P)$ is the slit orientation, and $\P$ is the path parameter (see Fig. 13-10b). The Helmholtz equation in a non-inertial reference frame rotating with $\Omega(\P)$, is $(\nabla^2 + k^2 - 2\pm\Omega k)E_\pm = 0$, where $E_\pm = 2^{-½}(E_x + i\pm E_y)$ are the eigenvectors of circular polarizations. Note that a spin-dependent Coriolis term appears in the corrected Helmholtz equation. This equation can be written as $(\nabla^2 + K^2)E_\pm = 0$, where $K(\mu) \approx k(\mu) - \pm\Omega$ is the *generalized momentum* [47,48,53]. A similar term also appears in the time-independent Schrödinger equation in the presence of a vector potential. This spin-dependent wavevector modification is a manifestation of the optical spin-orbit interaction similar to the spin-Hall and the Stern-Gerlach effects. The additional momentum leads to a geometric phase accumulation of,

$$¤_g = -\int \pm\Omega\, d\P = -\pm\bar{} \quad . \tag{13-3}$$

Accordingly, the phase of the scattered plasmonic wave will be continuous up to the factor of $2®$ everywhere excluding the point $r = 0$, where the phase dislocation appears. The phase in Eq. (13-3) is analogous to the phase arising in a AB wavefunction, $\cdot(\mathbf{r})$ [48,49]. The latter effect appears when a beam of particles with charge of q is scattered from an infinite impenetrable cylinder containing a magnetic flux $\Phi = \oint \mathbf{A}(\mathbf{r}) \cdot d\mathbf{r} = \iint \mathbf{B}(\mathbf{r})\, d\mathbf{S}$, where $\mathbf{A}(\mathbf{r})$ is the vector potential and $\mathbf{B}(\mathbf{r})$ is the magnetic field. The suitable vector potential is given by $\mathbf{A}(\mathbf{r}) = (\Phi/2®r)\,\hat{}$, where $\hat{}$ is the unit vector in the azimuthal direction. The corresponding time-independent Schröedinger equation is then given by, $\frac{1}{2m}\left(-i\hbar\nabla - q\mathbf{A}(\mathbf{r})\right)^2 \cdot (\mathbf{r}) = \frac{\hbar^2 k^2}{2m} \cdot (\mathbf{r})$, where m is the particle's mass and $\hbar$ is Plank's constant. Note that the expression in parentheses is the generalized momentum term. In the linear approximation in $\mathbf{A}$, the above equation can be written

as, $\left(\nabla^2 + k^2 - \frac{2iq}{\hbar}\mathbf{A}\cdot\nabla\right)\cdot(\mathbf{r}) = 0$. The resulting equation resembles the Helmholtz equation in the rotating frame, where the third term in the parentheses stands

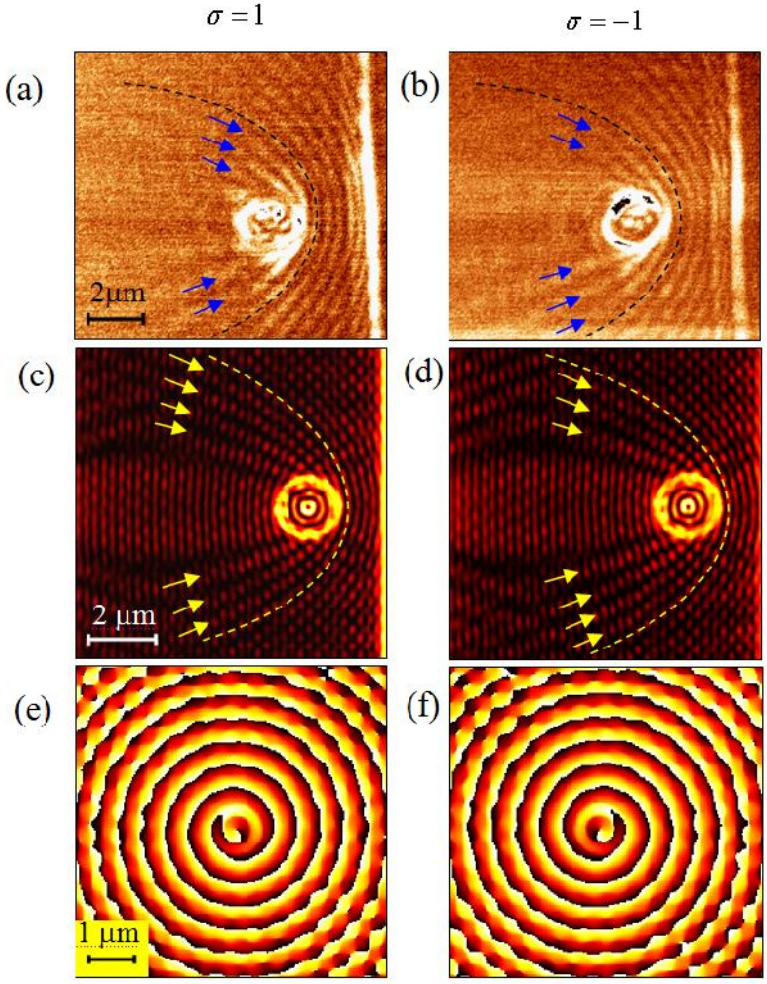

Fig. 13-11 a) and b) Measured intensity distribution of the SPPs scattered from a larger diameter defect compared to Fig. 13-10 (see text for details) for $\pm = 1$ and $\pm = -1$ polarizations, respectively, at $^{a} = 800nm$. c) and d) The calculated interference intensity distribution for $\pm = 1$ and $\pm = -1$, respectively, with the same defect as in a), now with $^{a} = 532nm$. To guide the eye, the dashed lines in a) – d) indicate one solid fringe and the arrows indicate the fringes appearing to the left of the dashed line. e) and f) The calculated phase distributions of the SPPs scattered from the same circular slit as in c) and d).

for the Coriolis term. In our system, the momentum correction term along the ¶ coordinate is $(\Delta k)_{\P} = \pm / r$, and is analogous to the $q\mathbf{A}$ term in the AB effect. The main result of the AB experiment is a spiral phase $¤ = \sim ¨$ acquired by the particles scattered from the cylinder, where the topological charge $\sim = q\Phi/(2®\hbar)$ is the magnetic flux parameter. The topological charge of the phase obtained in our experiment can be found as, $l = \frac{1}{2®}\oint (\Delta k)_{\P}\, d\P = \pm$. Therefore, one can conclude that the intrinsic spin in our experiment corresponds to the flux parameter $\sim$ in the AB effect. Due to the non-zero topological charge ($\pm = \pm 1$) a singularity of the plasmonic field appears in the center of the defect, resulting in a dark spot (see inset Fig. 13-10b). The vanishing electromagnetic field in the center corresponds to the impenetrability of the cylinder proposed in the AB experiment. Accordingly, the geometry of our system affects the resulting plasmonic phase front in a similar way as a vector potential affects the electrons' wavefunction. In contrast to the original AB effect, here the topological charge of the plasmonic spiral phase is spin-dependent, therefore it can be regarded as the intrinsic AB effect similar to the Aharonov-Casher effect [54].

A peculiarity of the observed effect lies in its geometric nature. The spiral phase of the plasmonic waves arises solely due to a rotation of the local anisotropy and is not the result of an optical path difference. Therefore, the phase dislocation will be independent of the wavelength or the size of the defect. This is confirmed experimentally on several elements with apertures of different sizes. Figure 13-11a,b presents the observed fringe patterns for circular slit with a diameter of 1.8 μm and width of 320 nm illuminated with $ª = 800nm$. Moreover, a FDTD simulation for the same defect size, but for $ª = 532nm$ incident illumination is presented in Fig. 13-11(c,d). In the measured as well as in the calculated near-field intensity distributions, same spin-dependent phase dislocations are clearly observed. A phase distribution of the scattered plasmonic field (without interfering with a reference wave) calculated by FDTD for $ª = 532nm$ illumination is presented in the Fig. 13-11e,f. The topological charge of the calculated spiral phase is equal to the incident spin and is not dependent upon the incident wavelength or the defect size, emphasizing the geometric nature of the observed effect. In the next section we will study the collective behavior of the defects upon the surface plasmon supporting media.

13.5 Spin-Dependent Plasmonics: Interfering Topological Defects

The results of the previous section show that the electromagnetic field scattered from subwavelength nanoaperture has an essential property of a topological defect (TD). The TD is a singular spatial configuration of a vector field which cannot unwind under continuous deformations [55] . Topological defects (TDs) are

among the most intriguing signatures of symmetry breaking in the laws of physics

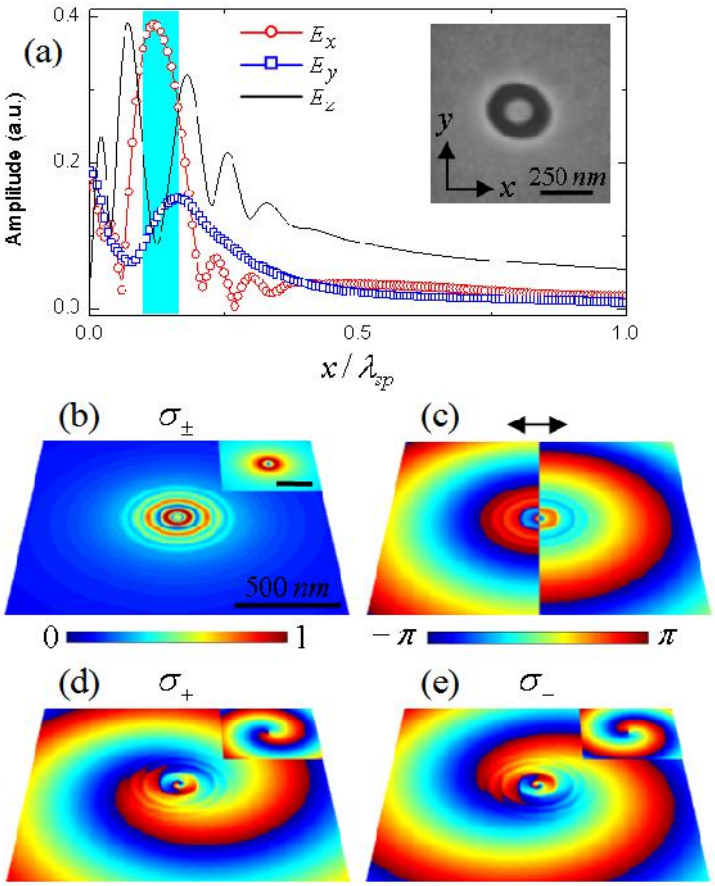

Fig. 13-12 Plasmonic vortex source. a) Horizontal cross sections of the near-field electromagnetic fields of the nanoantenna, normally illuminated with circularly polarized light, at a wavelength of 780 nm; the blue area corresponds to the width of the etched circular nanoslit. The inset shows a SEM image of an annular nanoantenna with inner and outer radii of 75 and 125 nm, respectively, upon a 200 nm thick Au film. b) FDTD simulation of the E_z magnitude for $\pm_{\pm}$. c) FDTD simulation of the E_z phase for horizontally linear polarization. d, e) FDTD simulations of the E_z phases for $\pm_{\pm}$, respectively. The insets in panels b, d and e show the corresponding analytical calculation.

[54]. TDs have attracted extensive attention in various realms such as condensed matter physics [57,58], superfluidics [59], hydrodynamics [60], cosmology [61], liquid crystals [62], and optics [63]. The optical TDs are termed vortices and they

carry an OAM of $l\hbar$ per photon manifested by the spiral phase $l¨$ of the beam, where the integer number l is the topological charge and ¨ is the azimuthal an gle. Observation of TDs in plasmonic systems is possible via the spin-orbit interaction (SOI), which provides a suitable mechanism to couple the optical spin to an OAM carried by the surface plasmons (SPs). Moreover, a measurement of a wavefront phase dislocation due to the scattering of SPs from a macro-wavelength TD was recently presented [64].

When a linearly polarized light illuminates a local scatterer, a typical dipolar SP polariton emission pattern is observed, aligned with the incident polarization direction [65,66], and comprises a perpendicular dislocation line. The scattering of the SP waves propagating away from the point scatterer is described as a source of spherical (Huygens) wave [66], with ® -phase retardation between the two sections intersected by the dislocation line (Fig. 13-12c). In this section we consider a spin-dependent plasmonics as result of scattering the circularly polarized wave from local defect on surface maintaining SP [67]. We choose an annular nanoslit as a source for a propagating plasmonic wavefront.

A FDTD simulation gives the near-field electromagnetic fields distribution for annular nanoantenna (Fig. 13-12a, inset), illuminated with a circular polarization. Figure 13-12a shows the horizontal cross sections of the electric field components. In the vicinity of the slit, all the field components have comparable amplitudes, while those components in the out-launching plasmonic wave decay in a different manner. After propagation to a distance of half a plasmonic wavelength, the contribution of the normal E_z component to the intensity distribution is an order of magnitude larger than those of the E_x and E_y components. Hence, for multi-wavelength propagation distances, the complex plasmonic wavefront launched from the nanoantenna mainly contains the E_z signature. Figure 13-12b shows the spin-degenerated magnitude of the electric field component E_z with zero-field amplitude in the origin. Moreover, the phase of the E_z field is spiral and its helicity is spin-dependent (Figs. 13-12d,e), resulting from the optical SOI. Due to the SOI, the excited SPs acquire an OAM which is equal to the incident spin, resulting in a nanoscale TD: a plasmonic vortex source.

We give below the analytical evaluation result for the E_z field launched from an annular nanoantenna - infinitely thin circular slit with a radius r_0, in a medium supporting SPs. The selected shape of the nanoantenna as a circular nanoslit originates from the simple boundary conditions formulation. A one-dimensional nanoslit provides a momentum modification in the perpendicular direction, which is essential for the coupling of light to non-radiative surface modes, thereby exciting a surface wave with a phase front parallel to the slit. Moreover, only transverse magnetic polarized incident waves with an electric field perpendicular to the slit are efficiently coupled by the slit to SPs. If we consider a circularly polarized light

as a rotating in time linear polarization, the maximal coupling efficiency along a circular nanoslit follows the local polarization selectivity of the one-dimensional slit [46]. The phase delay due to the varying polarization state results in a geometric phase, leading to a plasmonic field $E_z(r_0,\varphi) = \exp(-i\sigma\varphi)$, where σ is the incident spin. Two additional boundary conditions are required: zero-field amplitude at the origin and at infinity, arising from the spiral phase and a single point source, respectively.

The two-dimensional Helmholtz equation, with the SP wave vector k_{sp}, is separable in polar coordinates (r,φ), where r is the radius and φ is the azimuthal angle. The different boundary conditions for the internal and external regions dictate different solutions for the in- and out-propagating plasmonic fields. The resulting solution of the in- and out-propagating plasmonic fields are

$$E_z(r,\varphi) = \begin{cases} J_{-\sigma}(k_{sp}r)\left[J_{-\sigma}(k_{sp}r_0)\right]^{-1}e^{-i\sigma\varphi}, & in-wave \\ H_{-\sigma}(k_{sp}r)\left[H_{-\sigma}(k_{sp}r_0)\right]^{-1}e^{-i\sigma\varphi}, & out-wave \end{cases}$$

Here, J_m and H_m are the mth-order of the Bessel and Hankel functions of the first kind, respectively. The analytical results, presented in the insets of Figs. 13-12b,d,e, confirm the scattering dynamics of the SPs from the localized vortex source obtained by the FDTD simulations.

The described mechanism of spin degeneracy removal in a single nanoantenna paves the way for consideration of spin-dependent plasmonic devices based on multiple plasmonic vortex sources. In conventional optics, the point spread function (PSF) is given by the spherical wave $h \propto \exp(ikr)$, and it links between the input and output of a space-invariant system via the superposition (convolution) integral. We herein propose the spin-orbit PSF – a spiral wavefront $h_\sigma \propto \exp(-i\sigma\varphi)$ – where the incident spin is a degree of freedom. Hence, for a system consisting of multiple TD sources with an input g_1, the system output g_2 is spin-dependent and is described by the convolution relation $g_2(\sigma) = g_1 \otimes h_\sigma$. This concept encourages one to demonstrate different configurations of sources arrangements to observe *spinoptical* effects.

The experimental observation of multiple TD plasmonic field was completed on a circular chain of nanoscale TDs, etched by FIB at a thin Au film deposited on a glass substrate (Fig. 13-13a). The element was illuminated by a laser via a circular polarizer, and the excited SP wave was directly probed by the 150 nm aperture near-field scanning optical microscopy (NSOM) tip. The measured spin-degenerated intensity distribution is presented in Fig. 13-13b; the inset of Fig. 13-13a shows a horizontal cross section of the measured intensity and analytically calculated interference pattern of isolated TDs, at the center of the chain. A plasmonic interference pattern with a dark spot in the center (Fig. 13-13b, inset) is observed for the distinct spin states; such a singularity indicates a non-zero OAM,

corresponding to a spiral phase. The calculated phase distributions by the model for multiple plasmonic vortex sources are presented in Figs. 13-13c,d and verified its spin-dependent helicity. Moreover, this calculation provided the quantitative value of the OAM per photon, shown to be equal to the incident optical spin; therefore, the superposition of vortex sources in a circular symmetry results in an intensity-enhanced plasmonic vortex with a higher total OAM. Note that if spherical waves from point sources are considered, a bright spot at the center would be expected.

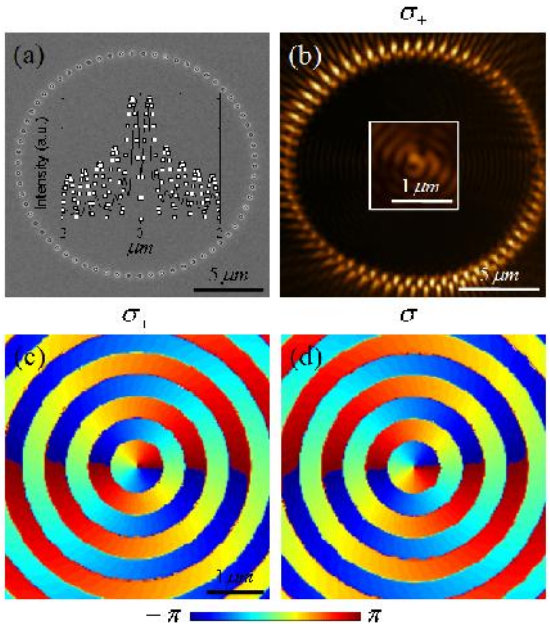

Fig. 13-13 Circular plasmonic chain of TDs. a) SEM image of the chain consisting of annular nanoapertures arranged in a circular path with a radius of 8 μm, and with a period of 760 nm. The inset shows a horizontal cross section of the intensity at the center of the chain; the curve and the squares represent the measured and analytically calculated intensities, respectively. b) Measured near-field intensity distribution for normally incident $\pm_{\pm}$ at a wavelength of 780 nm; the inset represents a magnification of the dark spot. c), d) Analytical calculations of the phase distributions of the plasmonic fields for $\pm_{\pm}$, respectively.

The total field of uncoupled plasmonic nanoantennas, separated by a distance of the SP wavelength, is the coherent summation of all the elemental fields. The absence of a collective coupling between TDs in the proposed plasmonic device was verified by FDTD simulations of the same geometry with a random distribution of nanoantennas; the similar spin-based effect observed in ordered and disor-

dered chains (not shown) is a signature for the non-collective behavior of the localized modes in the near-field. The isolated nature of TDs in the near-field is the basis for the multi-source consideration as the interference of vortex sources, and shows a good agreement with the spin-dependent experimental results

Another interesting spin-dependent plasmonic device based on the interference of TDs is a plasmonic focusing lens. A semicircular plasmonic chain consisted of annular nanoapertures with the previous parameters is shown in Fig. 13-14a. Figures 13-14c,d present the measured intensities of the focusing plasmonic waves

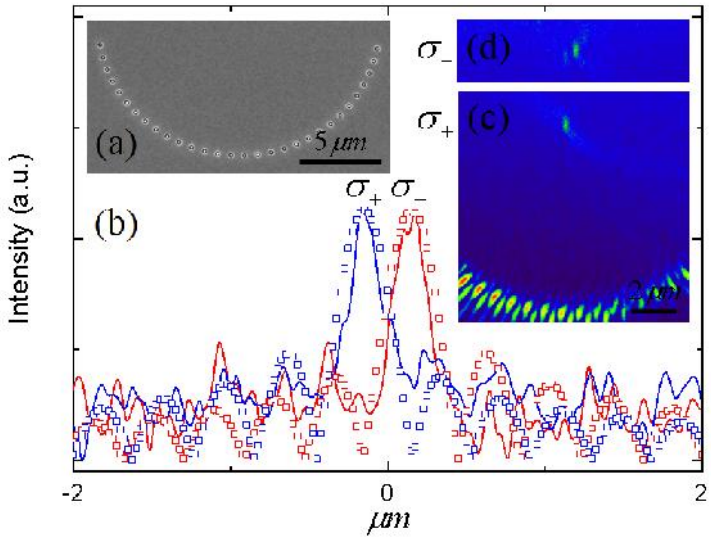

Fig. 13-14 Spin-dependent plasmonic focusing lens. a) SEM image of the plasmonic lens consisting of annular nanoapertures arranged in a semicircular path. b) Transverse cross sections of the intensity distributions in the focal plane; the blue and red curves (squares) represent the measured (analytically calculated) intensities for $\pm_{\pm}$, respectively. c), d) Measured near-field intensity distributions of the plasmonic lens, at a wavelength of 780 nm for normally incident $\pm_{\pm}$, respectively.

for $\pm_{\pm}$, respectively. A spin-dependent transverse shift of the focal spot is easily observed from the compared cross sections (Fig. 13-14b). The obtained focal shift is a manifestation of the *optical spin-Hall effect* [15,16,35,68], associated with the SOI, inducing the plasmonic vortex sources. The relocation of the spot can be calculated using the optical path condition with a spiral wavefront

$k_{sp} r_i - \pm^{\cdot\cdot}{}_i = 2\circledR m$, where r_i is the distance between the i th source and the shifted spot, $\cdot\cdot_i$ is the corresponding azimuthal angle, and m is an integer. Using this formalism, we estimate the spin-dependent deflection by $\pm / k_{sp}$ (~120 nm), and it evidently supports the experimental results as well as the analytical calculations (Fig. 13-14b). Moreover, the calculation of the plasmonic fields reveals $\circledR$ -phase retardation between the spin-dependent focusing waves. Hence, when the superposition of the spin states $2^{-1/2}\left(|\pm_+\rangle + |\pm_-\rangle\right)$ – a horizontal linear polarization – is illuminated, the focal spot splits in the lateral direction [64,35]; however, for the superposed excitation $i2^{-1/2}\left(|\pm_+\rangle - |\pm_-\rangle\right)$ – a vertical linear polarization – the retardation is compensated, and as a result the plasmonic wave homogeneously converges without a focal spot splitting [64].

In the next section we will introduce the optical spin-Hall effect induced by nanoapertures chain which observed in the far-field [35]

13.6 Optical Spin-Hall Effect from Plasmonic Nanoapertures

In contrast to the results of the previous section here we consider collective interaction within periodic plasmonic chains, which play a crucial role in the recoupling of SPs to a propagating mode via the momentum-matching condition, as was recently presented [35].

One can distinguish between two types of optical spin-Hall effect (OSHE) [35]. The *locally isotropic* optical spin-Hall effect (OSHE-LI) is regarded as the interaction between the optical spin and the path $\P$ of the plasmonic chain with an isotropic unit cell (Fig. 13-15a). In contrast, the *locally anisotropic* optical spin-Hall effect (OSHE-LA) occurs due to the interaction between the optical spin and the local anisotropy of the unit cell, which is independent on the chain path (Fig. 13-15b). This resembles two types of spin-Hall effects in electron 2D systems - intrinsic (due to Rashba coupling) and extrinsic (due to the spin-orbit-dependent scattering of electrons from impurities).

The OSHE-LI can be observed on a chain of scatterers whose local orientation with respect to the selected x coordinate $^- = \tan^{-1}(dy/dx)$ varies linearly with x, explicitly, $^-(x) = \circledR x/a$ where a is the period of the structure (Fig. 13-16b). This demand leads to a chain with a route $\{x(\P), y(\P)\}$ given by the function

$$\P = (a/2\circledR)\ln\left[\left(1+\sin\frac{\circledR x}{a}\right)\Big/\left(1-\sin\frac{\circledR x}{a}\right)\right]. \qquad (13\text{-}3)$$

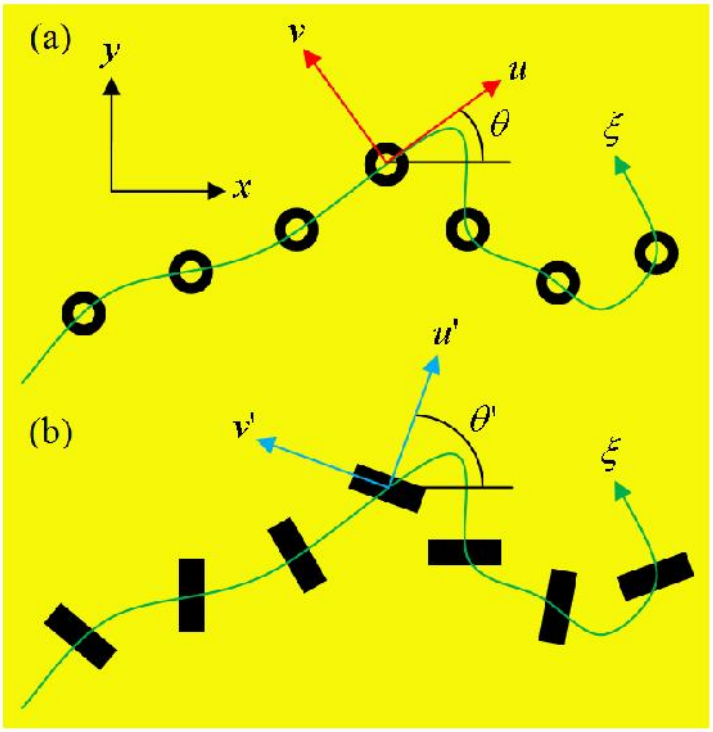

Fig. 13-15 Coupled localized plasmonic chains. a) A plasmonic chain with isotropic unit cell and rotating reference frame (u,v) which follows the path ¶ . b) An anisotropy unit cell chain with a frame (u',v') attached to the local anisotropy axis of the unit cell. The lab reference frame is indicated by (x,y).

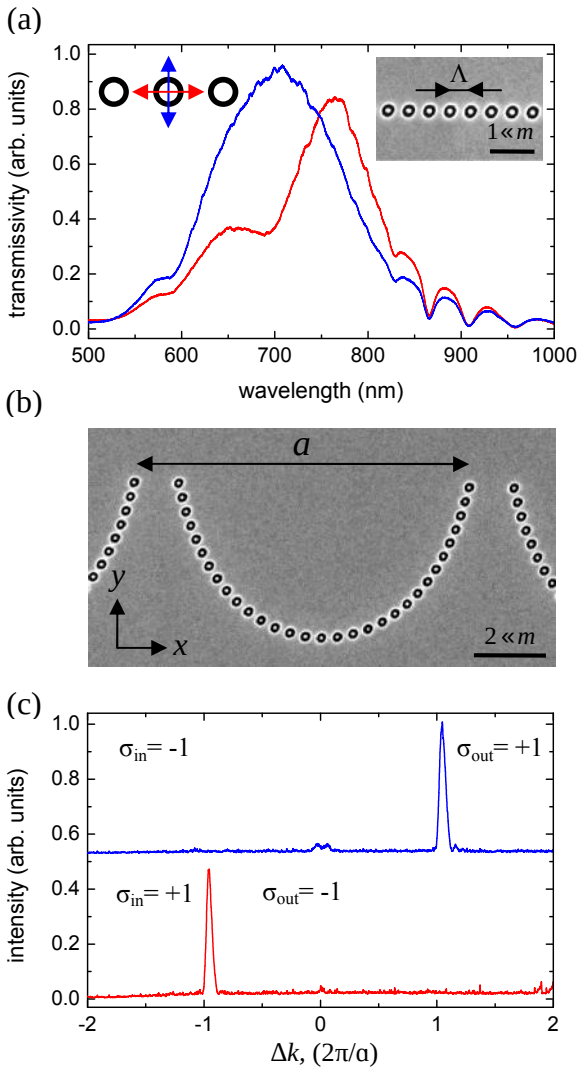

Fig. 13-16 a) Transmission spectra of the plasmonic chain consisting of coaxial nanoapertures with inner/outer radii of 75/125 nm, with period of $\Lambda = 470\,nm$ and a length of $84.6\,\text{«}m$. The blue and red lines/arrows correspond to transversal and longitudinal polarization excitations, respectively. The inset shows SEM image of the chain. b) SEM image of a curved chain whose local orientation ¯ is varied linearly along the *x*-axis with a rotation period of $a = 9\,\text{«}m$, and a structure length of $135\,\text{«}m$. c) The spin-dependent momentum deviation for the OSHE-LI, at a wavelength of 780 nm. The red and blue lines stand for incident right- and left-handed circularly polarized light, respectively ($\pm_{in} = \pm 1$). $\pm_{out}$ denotes the spin state of the scattered light.

The transmission spectrum of the coupled plasmonic chain, immersed in an index-matching oil to obtain symmetric configuration, bears a signature of two modes centered at the wavelengths of 700 and 780 nm corresponding to transversal and longitudinal polarization excitations [70], respectively (Fig. 13-16a).

Figure 13-16c shows the measured OSHE-LI observed from the chain corresponding to Eq. (13-3). In experiment the structure was sandwiched between circular polarizers and illuminated with a laser beam at a wavelength of 780 nm in order to excite the longitudinal mode. The intensity distribution is measured in the far-field, which corresponds to the momentum space.

Polarization analysis reveals that the scattering from the curved chain comprising two components: ballistic and spin-flip. The ballistic component doesn't experience any diffraction and maintains the polarization state of the incident beam, while the spin-flip component, with an opposite spin state, undergoes diffraction.

Spin-dependent beam deflection is observed in the experiment via orthogonal circular polarizers, corresponds to a momentum shift of $\Delta k_x = -2\pm ®/a$, where $\pm$ is the incident spin state. The peculiarity of the observed effect lies in its geometric nature. Light scattering by a system with spatially non-uniform anisotropy has a close analogy with a scattering from a revolving medium [39], as was shown recently [38]. Hence, the scattering by the bent chain is most conveniently studied using a rotating reference frame [52,38] (u,v), which is attached to the axis of the local anisotropy of the chain and follows the chain's route $¶(x,y)$ (Fig. 13-15a). This is accompanied by spatial rotation of the frame with a rate $\Omega_¶ = d^-(¶)/d¶$, where $^-(¶)$ is the orientation angle. As a result, a spin-dependent momentum deviation $\Delta k_¶ = -2\pm\Omega_¶$ which corresponds to an additional phase of $¤ = \int \Delta k_¶ \, d¶ = -2\pm^-$, appears in the spin-flip scattered component. The experimentally observed spin-Hall momentum deviation concurs with the expected correction of $\Delta k_x = \nabla_x ¤ = -2\pm ®/a$. This effect is regarded as the OSHE-LI.

When the chain unit cell is anisotropic itself, the local anisotropy is also allowed to be arbitrarily oriented along the path. The reference frame attached to the unit cell anisotropy is presented as the system (u',v') in Fig. 13-15b. It was previously shown that plasmonic structures consisting of nanorods exhibit a high polarization anisotropy that follows the orientation of the rods [71,72]. An element consisting of randomly arranged but similarly oriented rectangular apertures with dimensions of 80x220 nm (Fig. 13-17a, top inset) demonstrates the localized mode resonance at a wavelength of 730 nm by measuring the transmission spectrum with linear polarization excitation parallel to its minor axis. High anisotropy is clearly observed between the two orthogonal linear polarization excitations, which results from the local anisotropy of the nanorod (Fig. 13-17a). A straight chain of subwavelength nanorods with a period of 430 nm (Fig. 13-17a, bottom inset) gives

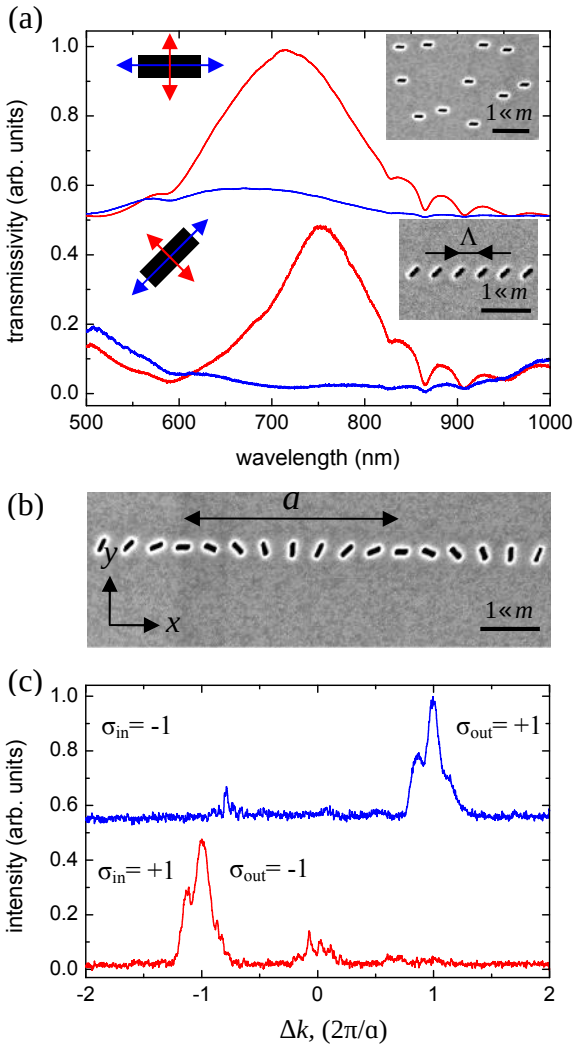

Fig. 13-17 a) Transmission spectra of randomly arranged identically oriented rectangular apertures with dimensions of 80x220 nm in $86\,\mu m$ square array, and of a homogeneous chain with period $\Lambda = 430\,nm$, local orientation $\theta = 45°$ and a length of $86\,\mu m$. The red and blue lines/arrows correspond to linear polarization excitations parallel and perpendicular to the nanorod's minor axis, respectively. The insets show SEM images of the structures described above. b) SEM image of a chain in which the nanorods' orientation θ varies linearly along the *x*-axis with a rotation period of $a = 3.44\,\mu m$, and a structure length of $86\,\mu m$. c) The spin-dependent momentum deviation for the OSHE-LA, at a wavelength of 730 nm. The red and blue lines stand for incident spin states $\pm_{in} = \pm 1$, respectively.

a narrow resonant line shape of the transmitted light in correspondence with the momentum matching condition, when the structure is illuminated by a linear polarization parallel to the nanorod's minor axis (Fig. 13-17a). When the orientation of the nanorods is varied linearly along the *x*-axis to obtain a spatial rotation rate of $\Omega = d^{-}{}'/dx = ®/a$ (Fig. 13-17b), the beam deflection of the spin-flip component

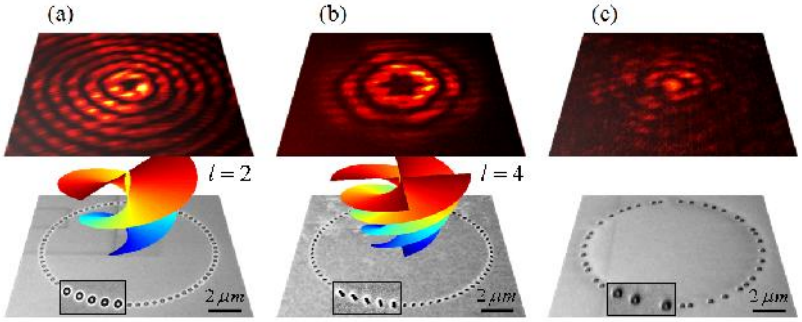

Fig 13-18 The OSHE-LI and OSHE-LA for circular chains. The measured far-field intensity distribution of the spin-flip component scattered from a circular chain of ordered a) and disordered c) coaxial apertures at a wavelength of 780 nm, and rotating nanorods with $m = 2$ at a wavelength of 730 nm b); bottom, SEM images of the chains with radii of $r_o = 5 « m$. The spin-Hall momentum deviation is accompanied by a spiral phase-front with $l = 2$ and $l = 4$, for the OSHE-LI (a) and OSHE-LA (b), respectively. Note that no spin-Hall momentum deviation is observed from the disordered chain (c).

corresponding to the spin-Hall momentum deviation of $\Delta k_x = -2 \pm \Omega$ arises (Fig. 13-17c). This beam deflection is regarded as the OSHE-LA and it arises due to the rotation of the local unit cell's anisotropy rather than the chain path curvature.The described mechanism paves the way for one to consider other path symmetries. According to Noether's theorem, for every symmetry in dynamical system there is a corresponding dynamical conservation law [73]. When the structure symmetry, or more explicitly the chain path $¶(x, y)$, is circular, the corresponding conservation rule is for the angular momentum (AM). The AM of an optical beam can have two components: an intrinsic component that is associated with the handedness of the optical spin, and an extrinsic (orbital) component that is associated with its spatial structure. In an optical paraxial beam with a spiral phase distribution

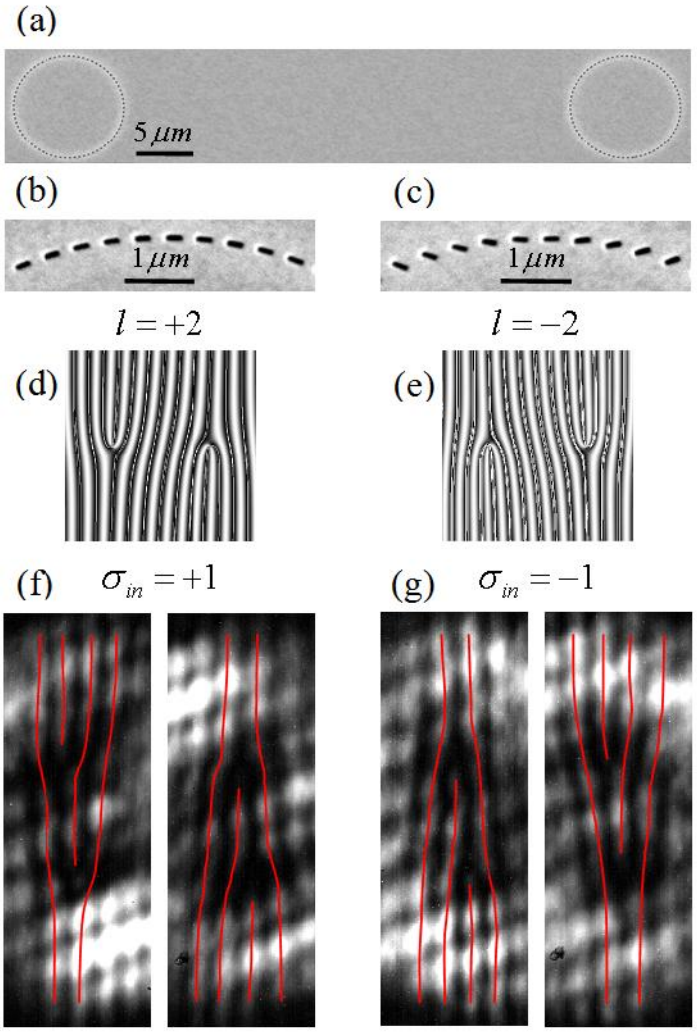

Fig 13-19 Dislocation's strength measurement. a) SEM image of two separated identical chains of nanorods rotated along a circular path with $m = 1$. b, c) Magnified segments of SEM images of circular chains with $m = \pm 1$, respectively. d, e) Calculated interference patterns for a pair of identical optical vortices with topological charges of $l = \pm 2$, respectively. f, g) Measured interference patterns of the spin-flip components for $m = 1$ (regions of interest), at a wavelength of 730 nm and incident spin states $\pm_{in} = \pm 1$, respectively. The additional fringes emerge above or below indicate the two generic phase dislocations and the red guiding lines emphasize their locations.

(¤ $= -l\ddot{}$, where $\ddot{}$ is the azimuthal angle in polar coordinates, and the integer number l is the topological charge), the total AM per photon, in units of $\hbar$ (normalized AM), was shown to be $j = \pm + l$ [33]. Let's consider circular chains with a path parameter ¶ $= r_o\ddot{}$ (r_o is the chain radius) of annular apertures and rotating nanorods with a rotation rate $\Omega = m/r_o$, so the local anisotropy orientation is $\bar{}' = m\ddot{}$ (m is an integer). The far-field intensity distributions of the scattered spin-flip components are presented in Figs. 13-18a,b for annular apertures and rotating nanorods with $m = 2$, respectively. A characteristic dark spot in the center is clearly seen in the images which is a signature of orbital AM. Moreover, it is evident that the radius of the dark spot for the nanorod chain of $m = 2$ is larger than the one for the annular apertures, corresponding to a higher orbital AM. The observed OSHEs and specifically the orbital AM obtained from circular chains are due to the collective interaction of the localized modes within the periodic plasmonic chains. The role of the interaction can be elucidated by comparing the spin-flip component of the scattered light from a circular chain with random distribution of annular apertures. As evident from Fig. 13-18c a bright spot was obtained, indicating zero orbital AM in a disordered plasmonic chain. The orbital AM of the spin-flip component scattered from a circular chain is characterized by the strength of the dislocation and its helicity. Phase dislocations are singular field points such that the phase obtains a 2® -fold jump when making a closed loop around them. The dislocation's strength is the number of wave-fronts that end at the phase dislocation point. Its absolute value and sign (helicity) can be measured simultaneously by the interference of two optical vortices [74,75]. For this purpose, one can use a system consisting of two separated identical chains of nanorods rotated along a circular path with $m = 1$ (Figs. 13-19a,b). The two chains, which behave as twin sources, give rise to intensity fringes, as shown in Figs. 13-19f,g. In the observed interference patterns of the spin-flip components, two additional fringes emerge, indicating two phase dislocations (see the guiding lines in Figs. 13-19f,g). When the incident spin state alters , the antisymmetric fork-like picture is reversed. The experimental patterns with an incident spin of $\pm = \pm 1$ are similar to the calculated patterns resulting from the scalar interference of two identical optical vortices with topological charges of $l = \pm 2$, respectively (Figs. 13-19d,e). The spin-dependent fringe patterns of a similar element with $m = -1$ (Fig. 13-19c) were also observed (not shown) to verify that the helicity of the phase dislocation corresponds to the rotation handedness of the nanorods. Moreover, the interference pattern of the ballistic component did not comprise a phase dislocation, indicating zero orbital AM. Each of the phase dislocations of the spin-flip components predicted by the calculated patterns (triple fork, see Figs. 13-19d,e), breaks in the experiment into a pair of fundamental phase dislocations (double fork, see Figs. 13-19f,g). The non-generic vortex collapse to generic vortices is in accordance with the prediction in Ref. [76]; therefore, the topological charge of the beam in this experiment is given by the number of the fundamental phase dislocations,

resulting in $l = \pm 2$. As the orbital AM is directly linked to the azimuthal momentum correction $\Delta k_{\cdot\cdot}$ via $l = -(1/2\circledR)\oint \Delta k_{\cdot\cdot}\, d\P$, the observed optical field with $l = 2m\pm$ provides the evidence for a spin-Hall momentum deviation of $\Delta k_{\cdot\cdot} = -2m\pm / r_o$. Since the unit cell anisotropy of the chain for $m = 1$ follows its curvature ($\bar{}' = \cdot\cdot$), the OSHE-LA in this case is equivalent to the OSHE-LI one. However, by *m*-fold rotation of the nanorods' orientation one can obtain *m*-fold magnification of the OSHE. Circular chains of annular apertures and rotating nanorods with $m = \pm 2$ were analyzed using the same interference method to experimentally demonstrate that the topological charge of the spin-flip component equals $l = 2\pm$ and $2m\pm$ for the OSHE-LI and OSHE-LA, respectively.

Finally, the topological charge's magnitude of the spin-flip component scattered from the circular chains can be verified by an interference, which results from a linear polarization projection of the ballistic and the spin-flip components [35]. For this purpose it is enough to measure the intensity distribution immediately behind the element via a linear polarizer. The interference patterns obtained

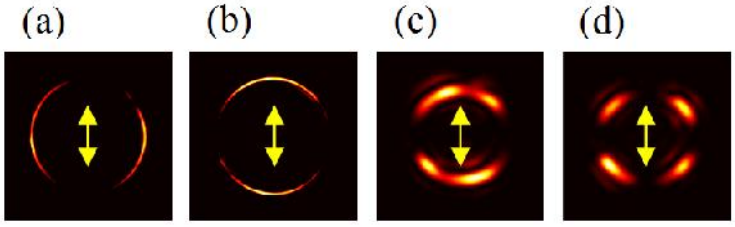

Fig 13-20 Interference patterns resulting from linear polarization projections of the ballistic and spin-flip components scattered from single circular chains of coaxial apertures (a, b), rotating nanorods with $m = 1$ (c) and $m = 2$ (d). The arrows indicate the direction of the linear polarizer-analyzer. The coaxial chain was illuminated at wavelengths of 780 and 700 nm to excite the longitudinal (a) and transversal (b) plasmonic modes, respectively. The nanorod chain was illuminated at 730 nm.

by circular chains of annular apertures and rotating nanorods with $m = 1, 2$ are visualized in Fig. 13-20. Propeller-like images confirm the orbital AM of *l*, which is expected from the obtained interference profile of $1 + \cos(l\cdot\cdot)$, for the OSHE-LI and OSHE-LA.

13.7 Coupled Thermal Antenna Lattices and Rashba-like Spin Degeneracy Violation

The spin state of elementary particles, atoms and molecules plays a key role in fundamental effects in physics. An external magnetic field causes energy separation of electrons (Zeeman effect) [77]. Spin-dependent momentum separation of charge carriers can occur due to structural inversion asymmetry in a material as result of spin-orbit interaction (Rashba and Dresselhaus effects) [78-80]. These two mechanisms show distinct patterns of energy dispersion, see Fig. 13-21. The photonic analogy of spin-orbit interaction is well known, wherein, the spin of the photons (helicity state of circularly polarized light) plays the role of the spin of charge carriers. Spin-dependent deflection of light was observed for propagation in gradient-index media [15, 53, 68] and with the scattering of surface plasmon polaritons (SPPs) from metallic nanostructures [34, 35, 46].

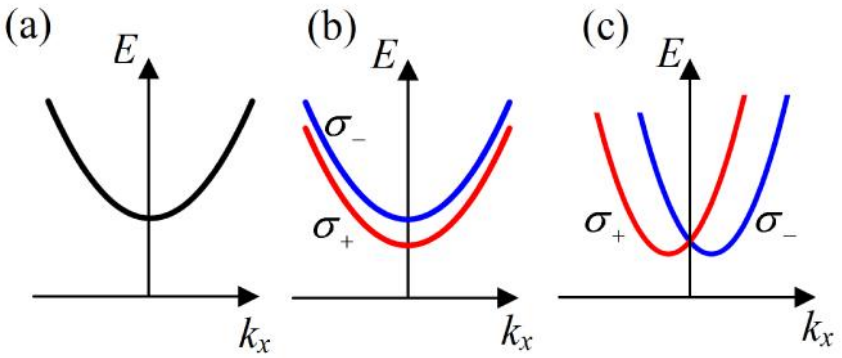

Fig. 13-21 Energy dispersion schemes of a) spin-degenerated system, b) energy splitting of the dispersion associated with Zeeman effect, c) spin-dependent shift of the dispersion in the momentum space.

When light is emitted or scattered from a revolving medium, it exhibits a dispersion splitting – angular Doppler effect (ADE) – which depends on the circular polarization handedness (the photon's spin) [39]. The dispersion splitting is attributed to a spin-dependent correction of the momentum term in the wave equation due to rotation of the emitting medium. In this section we will describe a spin-dependent dispersion splitting of *thermal radiation* emitted from a structure whose local anisotropy is rotated along selected *x*-axis. The observed effect is attributed to the dynamics of the thermally excited surface wave propagating along the structure [81].

For experiments the deepenings ("thermal antennas") with the subwavelength size of 1.2«m × 4.8«m (Fig. 13-22a, right inset)) were etched to a depth of 1«m on a SiC substrate forming isolated thermal antenna and coupled thermal antenna

array (Fig. 13-22c) with a period of $\Lambda = 11.6\ \mu m$. Two distinct resonances on isolated antenna, attributable to the local modes at $\mu_1/2® c = 885.7\, cm^{-1}$ and $\mu_2/2® c = 944.7\, cm^{-1}$, were observed at the temperature 773 K (Fig. 13-22a, curves I and II). These parameters find good agreement with calculations by the modified long wavelength approximation (MLWA) theory [82] resulting in $\mu_1^{(MLWA)}/2® c = 883.7\, cm^{-1}$ and $\mu_2^{(MLWA)}/2® c = 946.1\, cm^{-1}$ (Fig. 13-22b). Unlike the isolated antenna, the thermal antenna array manifest an additional narrow resonance peak at 830 cm^{-1}, attributed to collective antennas excitation (see Fig. 13-22a, curve III). The local resonances exhibit strong linear polarization along the direction of the small axis of the antenna. The emission dispersion measurement showed that the narrow spectral peak contains two propagating dispersive modes - a fast mode and a slow mode, (Fig. 13-23a) and the polarization direction of the slow mode follows the antennas' orientation (Fig. 13-23b).

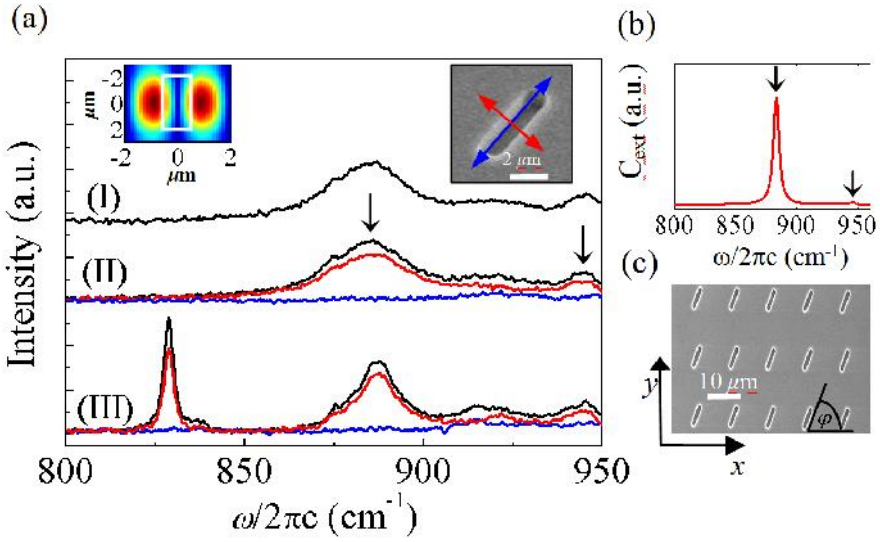

Fig. 13-22 a) Spectral emission from the isolated thermal antenna, measured at $^{-} = 6^{\circ}$ (I) and $^{-} = 0^{\circ}$ (II) [SEM image of the antenna, right inset], and for antenna array at $^{-} = 0^{\circ}$ (III) [SEM image in c)]; red and blue curves correspond to polarization along the short axis and long axis of the antenna, respectively, and the black for the total intensity. Left inset presents FDTD simulation of the intensity distribution in vicinity of an isolated antenna at 883.7 cm^{-1}, white square indicates the location of the antenna. Black arrows point to the local resonances. b) Calculated extinction cross section of an isolated antenna attained for polarization along the short axis of the antenna.

The polarization properties of the thermal antenna array dramatically and intriguingly change if orientation of antennas is gradually rotated along the *x*-axis. In

Fig. 13-24a the such antennas array with a distance along *x*-axis between neighboring antennas of Λ =11.6 μm is presented. The antennas' angle with respect to the x direction, $\ddot{}(x) = (\pi/a)x$, changes at a spatial rotation rate of $\Omega = d\ddot{}(x)/dx = ® /a$, where a is the distance along the x direction for a π rotation. Fig. 13-24b represents a spin-projected dispersion (in the k_x momentum direction) for a lattice with $\Omega = 0.17(® / \Lambda)$ obtained by measuring the S_3 component of the Stokes vectors, which represents the circular polarization portion within the emitted light.

In the measured dispersion of thermal radiation [81], the slow mode exhibits a clear spin-controlled splitting in the momentum of the emitted waves. The degree of splitting of these modes, $2\Delta k$, grows linearly with Ω, so as $\Delta k = \pm\,\Omega$, (Fig. 13-24c,d). The observed effect of the spin symmetry breaking is due to a spin-orbit

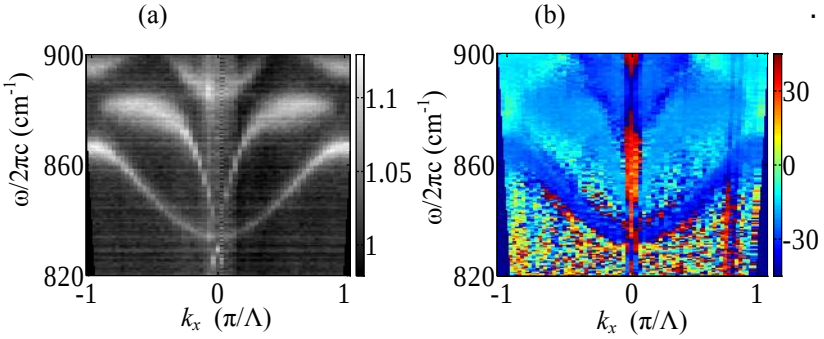

Fig. 13-23 a) Dispersion of thermal emission from the parallel antenna array ($\ddot{} = 60^o$); gray scale - intensity, a.u. b) Measured orientation angle of the polarization ellipse, ψ (°), for the dispersion in a).

interaction resulting from the dynamics of the surface waves propagating along the structure whose local anisotropy axis is rotated in space. The spin symmetry breaking is caused by the absence of inversion symmetry (IS) in the system. In general, time reversal symmetry (TRS) in a system results in energy relation $E(\mathbf{k},\pm_+) = E(-\mathbf{k},\pm_-)$. If the crystal lattice has inversion symmetry, i.e., the operation $\mathbf{r} \to -\mathbf{r}$ does not change the lattice, one will obtain $E(\mathbf{k},\pm_\pm) = E(-\mathbf{k},\pm_\pm)$. Consequently, if both TRS and IS are present, the band structure should satisfy the condition $E(\mathbf{k},\pm_+) = E(\mathbf{k},\pm_-)$. One can see that the inhomogeneous antenna lattice (Fig. 13-24a), has a broken inversion symmetry along the x direction, $\ddot{}(x) \neq \ddot{}(-x)$, resulting in $E(k_x,\pm_+) \neq E(k_x,\pm_-)$. However, from the dispersion depicted in Fig. 13-24b, it is evident that $E(k_x,\pm_+) = E(-k_x,\pm_-)$. Therefore, while

the system has broken IS, it preserves TRS. Such behavior is similar to the Rashba spin splitting in electron bands of heterostructures which stems from inversion asymmetry in the structure [79]. The momentum offset Δk in the Rashba effect is proportional to the Rashba parameter $\sim_R$, ($\Delta k = m^* \sim_R / \hbar^2$, m^* representing the effective mass of electrons), so in the observed photonic effect, the spatial rate of the lattices' inhomogeneity, Ω, resembles $m^* \sim_R / \hbar^2$. In the same manner, one can define a Rashba-like energy, E_{R-L}, ($E_{R-L} = \hbar \Delta\mu_{R-L}$, see Fig. 13-24c) that is proportional to Ω^2, in accordance with approximately parabolic shape of the slow modes.

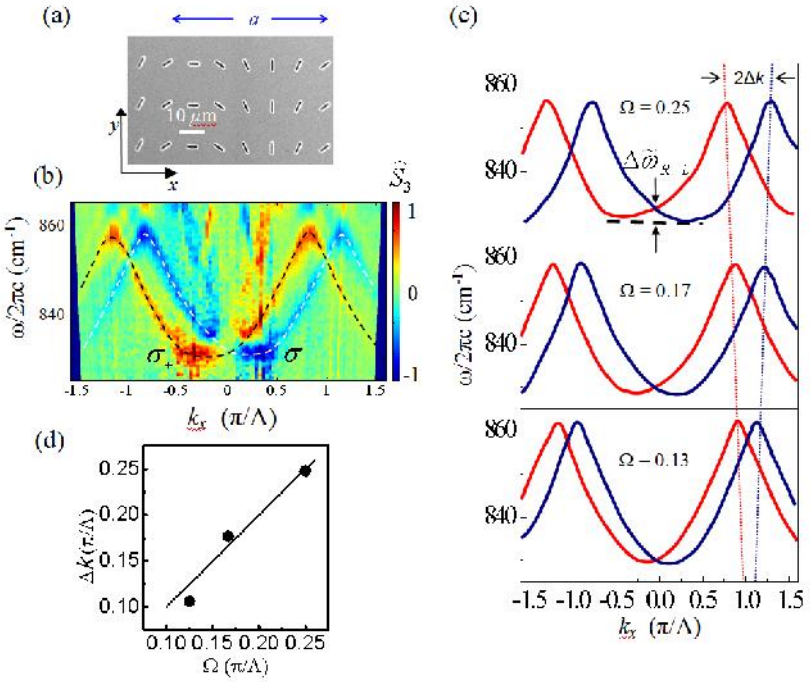

Fig. 13-24 a) SEM image of the lattice composed of antennas rotating along the *x*-axis with spatial rotation rate $\Omega = 0.17 (® / \Lambda)$. b) Measured spin-projected dispersion of emission from the lattice obtained by the Stokes parameter S_3 measurement; blue/red color corresponds to a negative/positive spin projection. Dashed white and black lines highlight the spin-split dispersion. c) Measured spin-projected dispersion of the split modes for various Ω (in units of $(® / \Lambda)$); red and blue lines correspond to $\pm_+$ and $\pm_-$ spin states, respectively; $\Delta\tilde{\mu}_{R-L}$ denotes the Rashba-like energy normalized by $\hbar / 2® c$. d) Observed

spin-controlled momentum displacement (circles), compared with the predicted dependence (solid line).

The peculiarity of the observed effect lies in its geometric nature. Surface waves scattered to radiation by a structure with spatially non-uniform anisotropy has a close analogy with emission from a revolving medium, as was recently shown [81]. Hence, the emission is most conveniently studied using a rotating reference frame that is attached to the axis of the local anisotropy of the antennas. The Helmholtz equation in a non-inertial reference frame revolving with rate $c\Omega << \mu$ is

$$(\nabla^2 + k^2 + 2\pm \Omega k)E_{\pm} = 0\,, \tag{13-4}$$

where $E_{\pm}$ are the eigenvectors of circular polarizations; note that $2\pm \Omega k$ is the Coriolis term. This equation similar to the Schrödinger equation $(\nabla^2 + k^2 + 2m^*{}_{R}\pm_{y}(-i\nabla)/\hbar^2)\Psi(r) = 0$ for the confined 1D Rashba system. The term $2m^*{}_{R}\pm_{y}(-i\nabla)/\hbar^2$ corresponds to the Coriolis term $2\pm \Omega k$, in accordance with our interpretation that Ω resembles $m^*{}_{R}/\hbar^2$. The equation (13-4) can be written as $\left(\nabla^2 + K^2\right)E_{\pm} = 0$, where $K(\mu) \approx k(\mu) + \pm \Omega$ is the generalized momentum, and the dispersion relation then becomes $\mu = \mu\left(k_x + \pm \Omega\right)$. Therefore, due to rotation of the local anisotropy axis, the original dispersion of the homogeneous lattice is now split into two modes with opposite spin states, each shifted by $\Delta k = \pm \Omega$ on the momentum axis. The corresponding generalized momentum is the manifestation of the spin-orbit interaction, which is responsible for effects such as the optical spin-Hall, Magnus, and Coriolis effects, and the Berry phase shift.

REFERENCES

[1] Ebbesen, T. W., Lezec, H. J., Ghaemi, H. F., Thio, T., Wolff, P. A.: Extraordinary optical transmission through sub-wavelength hole arrays. Nature **391**, 667-669 (1998).

[2] Lezec, H. J., Degiron, A., Devaux, E., Linke, R. A., Martin-Moreno, L., Garcia-Vidal, F. J., Ebbesen, T. W.: Beaming Light from a Subwavelength Aperture. Science **297**, 820-822 (2002).

[3] López-Tejeira, F., Rodrigo, S.G., *et al.*: Efficient unidirectional nanoslit couplers for surface plasmons. Nature Phys. **3**, 324-328 (2007).

[4] Yin, L., Vlasko-Vlasov, V. K., *et al*.: Subwavelength Focusing and Guiding of Surface Plasmons. Nano Lett. **5**, 1399-1402 (2005).

[5] Nomura, W., Ohtsu, M., Yatsui, T.:Nanodot coupler with a surface plasmon polariton condenser for optical far/near-field conversion. Appl. Phys. Lett. **86**, 181108-181111 (2005).

[6] Bozhevolnyi, S. I., Volkov, V. S., Devaux, E., Laluet, J. Y., Ebbesen, T. W.: Channel plasmon subwavelength waveguide components including interferometers and ring resonators. Nature **440**, 508-511 (2006).

[7] Gay, G., Alloschery, O., Viaris de Lesegno, B., Weiner, J., Lezec, H. J.: Surface Wave Generation and Propagation on Metallic Subwavelength Structures Measured by Far-Field Interferometry. Phys. Rev. Lett. **96**, 213901-4 (2006).

[8] Greffet, J.-J, Carminati, R., Joulain, K., Mulet, J.-P., Mainguy, S., Yong, C.: Coherent emission of light by thermal sources. Nature **416**, 61-64 (2002).

[9] Dahan, N., Niv, A., Biener, G., Gorodetski, Y., Kleiner, V., Hasman, E.: Enhanced coherency of thermal emission: Beyond the limitation imposed by delocalized surface waves. Phys. Rev. B **76,** 045427-5 (2007).

[10] Garcia-Vidal, F. J., Pendry, J. B.: Collective Theory for Surface Enhanced Raman Scattering. Phys. Rev. Lett. **77**, 1163-1166 (1996).

[11] Prosvirnin, S. L., Zheludev, N. I.: Polarization effects in the diffraction of light by a planar chiral structure. Phys. Rev. E **71**, 037603-4 (2005).

[12] Krasavin, A. V., Schwanecke, A. S., Zheludev, N. I.: Polarization conversion and "focusing" of light propagating through a small chiral hole in a metallic screen. Appl. Phys. Lett. **86**, 201105-3 (2005).

[13] Fang, N., Lee, H., Sun, C., Zhang, X.: Sub–Diffraction-Limited Optical Imaging with a Silver Superlens. Science **308**, 534-537 (2005).

[14] Smolyaninov, I. I., Hung, Y., Davis, C.: Magnifying Superlens in the Visible Frequency Range. Science **315**, 1699-1701 (2007).

[15] Bliokh, K. Y., Niv, A., Kleiner, V., Hasman, E.: Geometrodynamics of spinning light. Nature Photonics **2**,748-753 (2008).

[16] Gorodetski, Y., Niv, A., Kleiner, V., Hasman, E. Observation of spin-based plasmonic effect in nanoscale structures.: Phys. Rev. Lett. **101**, 043903-4 (2008).

[17] Barnes, W. L., Dereux, A., Ebbesen, T.W.: Surface plasmon subwavelength optics. Nature **424**, 824-30 (2003).

[18] Majorana, E.: Atomi orientati in campo magnetico variabile. Nuovo Cim. **9**, 43 (1932)

[19] Hannay, J. H.: The Majorana representation of polarization, and the Berry. phase of light. J. Mod. Opt. **45**, 1001-1008 (1998).

[20] Berry, M. V.: The adiabatic phase and Pancharatnam's phase for polarized light. J. Mod. Opt. **34**, 1401-1407 (1987).

[21] Bomzon, Z., Kleiner, V., Hasman, E.: Pancharatnam-Berry phase in space-variant polarization state manipulations with subwavelength gratings. Opt. Lett. **26**, 1424-1426 (2001);

[22] Bomzon, Z., Kleiner, V., Hasman, E.:Formation of radially and azimuthally polarized light using space-variant subwavelength metal stripe gratings. Appl. Phys. Lett. **79**, 1587-1589 (2001).

[23] Baranova, N. B., Savchenko, A. Yu., Zel'dovich, B. Ya.: Transverse shift of a focal spot due to switching of the sign of circular polarization. JETP Letters **59**, 232-235 (1994).

[24] Zel'dovich, B.Ya; Kundikova, N.D.; Rogacheva, L.F.: Observed transverse shift of a focal spot upon a change in the sign of circular polarization. JETP Letters, **59**, 766-769, (1994).

[25] Kavokin, A., Malpuech, G., Glazov, M.: Optical Spin Hall Effect. Phys. Rev. Lett. **95**, 136601-4 (2005).

[26] Leyder, C., Romanelli, M., Karr, J. Ph., Giacobino, E., Liew, T. C. H., Glazov, M. M., Kavokin, A. V., Malpuech, G., Bramati, A.: Observation of the optical spin Hall effect. Nature, **3**, 628-631 (2007).

[27] Gerlach, W., Stern, O.: Das magnetische Moment des Silberatoms. Z. Phys. **9,** 353–355 (1922).

[28] Zhou, F.: Topological spin pumps: The effect of spin rotation on quantum pumps. Phys. Rev. B **70**, 125321-18 (2004).

[29] Poynting, J. H. The wave motion of a revolving shaft, and suggestion as to the angular momentum in the beam of circularly polarised light. Proc. Roy. Soc. A **82**, 560-567 (1909).

[30] Beth, R. A. Mechanical detection and measurement of the angular momentum of light. Phys. Rev. **50**, 115-125 (1936).

[31] Van Enk, S. J., & Nienheuis, G. Eigenfunction description of laser beams and orbital angular momentum of light. Opt. Commun. **94**, 147-158 (1992).

[32] O'Neil, A. T., MacVicar, I., Allen, L., Padgett, M. J.: Intrinsic and extrinsic nature of the orbital angular momentum of a light beam. Phys. Rev. Lett. **88**, 053601-4 (2002).

[33] Allen, L., Beijersbergen, M. W., Spreeuw, R. S., Woerdman, J. P.: Orbital angular momentum of light and the transformation of Laguerre-Gaussian laser modes. Phys. Rev. A **45**, 8185-8190 (1992).

[34] Gorodetski, Y. N. Shitrit, I. Bretner, V. Kleiner, E. Hasman, "Observation of Optical Spin Symmetry Breaking in Nanoapertures". Nano Lett. **9**, 3016–3019 (2009).

[35] Shitrit, N., Bretner, I., Gorodetski, Y., Kleiner, V., Hasman, E.: Optical Spin Hall Effects in Plasmonic Chains. Nano Lett. , **11**, 2038-2042 (2011).

[36] Liberman, V. S., Zel'dovich, B. Ya. Spin-orbit interaction of a photon in an inhomogeneous medium. Phys. Rev. A **46**, 5199-5207 (1992).

[37] Niv, A., Gorodetski, Y., Kleiner, V., Hasman, E.: Topological spin–orbit interaction of light in anisotropic inhomogeneous subwavelength structures. Opt. Lett. **33**, 2910-2912 (2008).

[38] Bliokh, K. Y., Gorodetski, Y., Kleiner V., Hasman, E.: Coriolis effect in optics: Unified geometric phase and spin-Hall effect. Phys. Rev. Lett. **101**, 030404-4 (2008).

[39] Garetz, B. A.: Angular Doppler effect. J. Opt. Soc. Am. **71**, 609-611 (1981).

[40] Schwanecke, A. S., Fedotov, V. A., Khardikov, V. V., Prosvirnin, S. L., Chen, Y., Zheludev, N. I.: Nanostructured metal film with asymmetric optical transmission. Nano Lett. **8**, 2940-2943 (2008).

[41] Kuwata-Gonokami, M., Saito, N., Ino, Y., Kauranen, M., Jefimovs, K., Vallius, T., Turunen, J., Svirko, Y.: Giant optical activity in quasi-two-dimensional planar nanostructures. Phys. Rev. Lett. **95**, 227401-4 (2005).

[42] Drezet, A., Genet, C., Laluet, J-Y., Ebbesen, T. W.: Optical chirality without optical activity: How surface plasmons give a twist to light. Opt. Express **16**, 12559-12570 (2008).

[43] Ohno, T., Miyanishi, S.: Study of surface plasmon chirality induced by Archimedes' spiral grooves. Opt. Express, **14**, 6285-6290 (2006).

[44] Lockyear, M. J., Hibbins, A. P., Sambles, J. R., Lawrence, C. R.: Microwave Transmission through a Single Subwavelength Annular Aperture in a Metal Plate. Phys. Rev. Lett. **94**, 193902 (2005).

[45] Niv, A., Biener, G., Kleiner V., Hasman, E.: Manipulation of the Pancharatnam phase in vectorial vortices. Opt. Express **14**, 4208-4220 (2006).

[46] Gorodetski, Y., Nechayev, S., Kleiner, V., Hasman, E.: Plasmonic Aharonov-Bohm effect: Optical spin as the magnetic flux parameter. Phys. Rev. B , **82**, 125433-4 (2010).

[47] Aharonov, Y., Bohm, D.: Significance of Electromagnetic Potentials in the Quantum Theory. Phys. Rev. **115**, 485-491 (1959).

[48] Berry, M. V., Chambers, R. G., Large, M. D., Upstill, C., Walmsley, J. C.: Wavefront dislocations in the Aharonov-Bohm effect and its water wave analogue. Eur. J. Phys. **1**, 154-162 (1980).

[49] Coste, C., Lund, F., Umeki, M.: Shallow water Scattering of dislocated wave fronts by vertical vorticity and the Aharonov-Bohm effect. I. Phys. Rev. E. **60**, 4908-4916 (1999).

[50] López-Tejeira, F., Rodrigo, S. G., Martin-Moreno, L., Garcia-Vidal, F. J., Devaux, E., Ebbesen, T. W., Krenn, J. R., Radko, I. P., Bozhevolnyi, S. I., González, M. U., Weeber, J. C., Dereux, A.: Efficient unidirectional nanoslit couplers for surface plasmons. Nat. Phys. **3**, 324-328 (2007).

[51] Aigouy, L., Lalanne, P., Hugonin, J. P., Julié, G., Mathet, V., Mortier, M.: Near-Field Analysis of Surface Waves Launched at Nanoslit Apertures. Phys. Rev. Lett. **98**, 153902-4 (2007).

[52] Lipson, S. G.: Berry's phase in optical interferometry: a simple derivation. Opt. Lett. **15**, 154-155 (1990).

[53] Bliokh, K. Y.: Geometrodynamics of polarized light: Berry phase and spin Hall effect in a gradient-index medium. J. Opt. A: Pure Appl. Opt. **11**, 094009-14 (2009).

[54] Aharonov, Y., Casher, A.: Topological Quantum Effects for Neutral Particles. Phys. Rev. Lett. **53**, 319-321 (1984).

[55] Pugatch, R.; Shuker, M.; Firstenberg, O.; Ron, A.; Davidson, N.: Topological Stability of Stored Optical Vortices. Phys. Rev. Lett. **98**, 203601-4 (2007).

[56] Mermin, N. D.: The topological theory of defects in ordered media. Rev. Mod. Phys. **51**, 591-648 (1979).

[57] Saito, H., Kawaguchi, Y., Ueda, M.: Topological defect formation in a quenched ferromagnetic Bose-Einstein condensates. Phys. Rev. A, ***75***, 013621-10 (2007**)**.

[58] de Juan, F., Cortijo, A., Vozmediano, M. A. H., Cano, A.: Aharonov–Bohm interferences from local deformations in graphene. Nature. Phys., **7**, 810-815 (2011).

[59] Blaauwgeers, R., Eltsov, V. B.; Krusius, M., Ruohio, J. J., Schanen, R., Volovik, G. E.:Double-quantum vortex in superfluid ^{3}He-A. Nature , **404**, 471-473 (2000).

[60] Goren, G., Procaccia, I., Rasenat, S., Steinberg, V.: Interactions and dynamics of topological defects: Theory and experiments near the onset of weak turbulence. Phys. Rev. Lett., **63**, 1237-1240 (1989).

[61] Davis, R. L.: Texture: A cosmological topological defect. Phys. Rev. D, **35**, 3705-3708 (1987).

[62] Brasselet, E., Loussert, C.: Electrically controlled topological defects in liquid crystals as tunable spin-orbit encoders for photons. Opt. Lett., **36**, 719-721 (2011).

[63] Nye, J. F., Berry, M. V.: Dislocations in wave trains. Proc. R. Soc. London, Ser. A, **336**, 165-190 (1974)..

[64] Yin, L., Vlasko-Vlasov, V. K., Pearson, J., Hiller, J. M., Hua, J., Welp, U., Brown, D. E., Kimball, C. W.: Subwavelength Focusing and Guiding of Surface Plasmons. Nano Lett., **5**, 1399-1402 (2005).

[65] Laluet, J.-Y., Drezet, A.; Genet, C., Ebbesen, T. W.: Generation of surface plasmons at single subwavelength slits: from slit to ridge plasmon. N. J. Phys., **10**, 105014-9 (2008).

[66] Zia, R., Brongersma, M. L.: Surface plasmon polariton analogue to Young's double-slit experiment. Nature. Nanotechnol. , **2**, 426-429 (2007).

[67] Shitrit, N., Nechayev, S., Kleiner, V., Hasman, E.: Spin-Dependent Plasmonics Based on Interfering Topological Defects. Nano Letters **12**, 1620- (2012).

[68] Hosten, O., Kwiat, P.: Observation of the Spin Hall Effect of Light via Weak Measurements. Science, **319**, 787-790 (2008).

[69] Hentschel, M.; Saliba, M.; Vogelgesang, R.; Giessen, H.; Alivisatos, A. P.; Liu, N.: Transition from Isolated to Collective Modes in Plasmonic Oligomers. Nano Lett. , **10**, 2721-2726 (2010).

[70] Maier, S. A., Brongersma, M. L., Kik, P. G., Atwater, H. A.: Observation of near-field coupling in metal nanoparticle chains using far-field polarization spectroscopy. Phys. Rev. B , **65**, 193408-4 (2002).

[71] Gordon, R., Brolo, A. G.; McKinnon, A., Rajora, A., Leathem, B., Kavanagh, K. L.: Strong Polarization in the Optical Transmission through Elliptical Nanohole Arrays. Phys. Rev. Lett., **92**, 037401-4 (2004).

[72] Koerkamp, K. J. K., Enoch, S., Segerink, F. B., van Hulst, N. F., Kuipers, L.: Strong Influence of Hole Shape on Extraordinary Transmission through Periodic Arrays of Subwavelength Holes. Phys. Rev. Lett., **92**, 183901-4 (2004).

[73] Koralek, J. D., Weber, C. P., Orenstein, J., Bernevig, B. A., Zhang, S.-C., Mack, S., Awschalom, D. D.: Emergence of the persistent spin helix in semiconductor quantum wells. Nature , **458**, 610-613 (2009).

[74] Sztul, H. I., Alfano, R. R.: Double-slit interference with Laguerre-Gaussian beams. Opt. Lett., **31**, 999-1001 (2006).

[75] Brasselet, E., Murazawa, N., Misawa, H., Juodkazis, S.: Optical Vortices from Liquid Crystal Droplets. Phys. Rev. Lett., **103**, 103903-4 (2009).

[76] Soskin, M. S., Gorshkov, V. N., Vasnetsov, M. V., Malos, J. T., Heckenberg, N. R.: Topological charge and angular momentum of light beams carrying optical vortices. Phys. Rev. A, **56**, 4064-4075 (1997).

[77] Zeeman, P., On the influence of Magnetism on the Nature of the Light emitted by a Substance. Phil. Mag. **43**, 226-239 (1897).

[78] Rashba, E.I.: Properties of semiconductors with an extremum loop. 1. Cyclotron and combinational resonance in a magnetic field perpendicular to the plane of the loop. Sov. Phys. Solid State **2**, 1109 (1960).

[79] Ishizaka, K., Bahramy, M.S., Murakawa, H., Sakano, M., Shimojima, T., Sonobe, T., Kiozumi, K., Shin, S., Miyahara, H., Kimura, A., Miamoto, K., Okuda, T., Namatame, H., Taniguchi, M., Arita, R., Nagaosa, N., Kobayashi, K., Murakami, Y., Kumai, R., Kaneko, Y., Onose, Y., Tokura, Y.: Giant Rashba-type spin splitting in bulk BiTel.: Nature Mater. **10,** 521-526 (2011).

[80] Dresselhaus, G.: Spin–orbit coupling effects in zinc blende structures. Phys. Rev. **100**, 580–586 (1955).

[81] Dahan, N., Gorodetski, Y., Frischwasser, K., Kleiner, V., Hasman, E.: Geometric Doppler Effect: Spin-Split Dispersion of Thermal Radiation.: Phys. Rev. Lett. **105**, 136402-4 (2010).

[82] Ko, K.D., Toussaint Jr., C.K.: A simple GUI for modeling the optical properties of single metal nanoparticles. Journal of Quantitative Spectroscopy & Radiative Transfer **110**, 1037-1043 (2009).